The Astrophysical Journal, 923:258 (26pp), 2021 December 20 https://doi.org/10.3847/1538-4357/ac23c6

The Gravity Collective: A Search for the Electromagnetic Counterpart to the Neutron Star–Black Hole Merger GW190814

Charles D. Kilpatrick[1], David A. Coulter[2], Iair Arcavi[3,4], Thomas G. Brink[5], Georgios Dimitriadis[2], Alexei V. Filippenko[5,6], Ryan J. Foley[2], D. Andrew Howell[7,8], David O. Jones[2,58], Daniel Kasen[11,12,13], Martin Makler[9,10], Anthony L. Piro[14], César Rojas-Bravo[2], David J. Sand[15], Jonathan J. Swift[16], Douglas Tucker[17], WeiKang Zheng[5], Sahar S. Allam[17], James T. Annis[17], Juanita Antilen[18], Tristan G. Bachmann[19], Joshua S. Bloom[5,20], Clecio R. Bom[10,21], K. Azalee Bostroem[22], Dillon Brout[23,58], Jamison Burke[7,8], Robert E. Butler[24], Melissa Butner[25], Abdo Campillay[26], Karoli E. Clever[2], Christopher J. Conselice[27], Jeff Cooke[28,29], Kristen C. Dage[30,31,32], Reinaldo R. de Carvalho[33], Thomas de Jaeger[5,34], Shantanu Desai[35], Alyssa Garcia[36], Juan Garcia-Bellido[37], Mandeep S. S. Gill[38], Nachiket Girish[5], Na'ama Hallakoun[3,39], Kenneth Herner[17], Daichi Hiramatsu[7,8], Daniel E. Holz[40], Grace Huber[16], Adam M. Kawash[32], Curtis McCully[7,8], Sophia A. Medallon[2], Brian D. Metzger[41,42], Shaunak Modak[5], Robert Morgan[43], Ricardo R. Muñoz[18], Nahir Muñoz-Elgueta[44], Yukei S. Murakami[5], Felipe Olivares E.[45], Antonella Palmese[17], Kishore C. Patra[5], Maria E. S. Pereira[36], Thallis L. Pessi[46,47], J. Pineda-Garcia[48], Jonathan Quirola-Vásquez[49,50], Enrico Ramirez-Ruiz[2], Sandro Barboza Rembold[46], Armin Rest[51,52], Ósmar Rodríguez[3], Luidhy Santana-Silva[33], Nora F. Sherman[36], Matthew R. Siebert[2], Carli Smith[2], J. Allyn Smith[53], Marcelle Soares-Santos[36], Holland Stacey[16], Benjamin E. Stahl[5], Jay Strader[32], Erika Strasburger[5], James Sunseri[5], Samaporn Tinyanont[2], Brad E. Tucker[54,55,56], Natalie Ulloa[26], Stefano Valenti[22], Sergiy S. Vasylyev[5], Matthew P. Wiesner[57], and Keto D. Zhang[5]

[1] Center for Interdisciplinary Exploration and Research in Astrophysics (CIERA), Northwestern University, Evanston, IL 60208, USA; ckilpatrick@northwestern.edu
[2] Department of Astronomy and Astrophysics, University of California, Santa Cruz, CA 95064, USA
[3] The School of Physics and Astronomy, Tel Aviv University, Tel Aviv 69978, Israel
[4] CIFAR Azrieli Global Scholars program, CIFAR, Toronto, ON, Canada
[5] Department of Astronomy, University of California, Berkeley, CA 94720-3411, USA
[6] Miller Institute for Basic Research in Science, University of California, Berkeley, CA 94720, USA
[7] Department of Physics, University of California, Santa Barbara, CA 93106-9530, USA
[8] Las Cumbres Observatory, 6740 Cortona Drive, Suite 102, Goleta, CA 93117-5575, USA
[9] International Center for Advanced Studies and Instituto de Ciencias Físicas, ECyT-UNSAM & CONICET, 1650, Buenos Aires, Argentina
[10] Centro Brasileiro de Pesquisas Físicas, Rua Dr. Xavier Sigaud 150, CEP 22290-180, Rio de Janeiro, RJ, Brazil
[11] Department of Physics, University of California, Berkeley, CA 94720-3411, USA
[12] Department of Astronomy and Theoretical Astrophysics Center, University of California, Berkeley, CA 94720-3411, USA
[13] Nuclear Science Division, Lawrence Berkeley National Laboratory, Berkeley, CA 94720, USA
[14] The Observatories of the Carnegie Institution for Science, 813 Santa Barbara Street, Pasadena, CA 91101, USA
[15] Steward Observatory, University of Arizona, 933 North Cherry Avenue, Tucson, AZ 85721-0065, USA
[16] Thacher Observatory, Thacher School, 5025 Thacher Road, Ojai, CA 93023, USA
[17] Fermi National Accelerator Laboratory, P.O. Box 500, Batavia, IL 60510, USA
[18] Departamento de Astronomía, Universidad de Chile, Camino El Observatorio 1515, Las Condes, Santiago, Chile
[19] Department of Astronomy and Astrophysics, University of Chicago, Chicago, IL 60637, USA
[20] Lawrence Berkeley National Laboratory, 1 Cyclotron Road, MS 50B-4206, Berkeley, CA 94720-3411, USA
[21] Centro Federal de Educação Tecnológica Celso Suckow da Fonseca, Rodovia Mário Covas, lote J2, quadra J, CEP 23810-000, Itaguaí, RJ, Brazil
[22] Department of Physics and Astronomy, University of California, Davis, CA, 95616, USA
[23] Center for Astrophysics, Harvard & Smithsonian, 60 Garden Street, Cambridge, MA 02138, USA
[24] Department of Astronomy, Indiana University, 727 E. Third Street, Bloomington, IN 47405, USA
[25] Department of Physics and Astronomy, East Tennessee State University, Johnson City, TN 37614, USA
[26] Carnegie Observatories, Las Campanas Observatory, Casilla 601, La Serena, Chile
[27] Jodrell Bank Centre for Astrophysics, University of Manchester, Oxford Road, Manchester, UK
[28] Centre for Astrophysics and Supercomputing, Swinburne University of Technology, PO Box 218, H29, Hawthorn, VIC 3122, Australia
[29] Australian Research Council Centre of Excellence for Gravitational Wave Discovery, Swinburne University of Technology, Hawthorn, VIC 3122, Australia
[30] Department of Physics, McGill University, 3600 University Street, Montréal, QC H3A 2T8, Canada
[31] McGill Space Institute, McGill University, 3550 University Street, Montréal, QC H3A 2A7, Canada
[32] Center for Data Intensive and Time Domain Astronomy, Department of Physics and Astronomy, Michigan State University, East Lansing, MI 48824, USA
[33] NAT-Universidade Cruzeiro do Sul / Universidade Cidade de São Paulo, Rua Galvão Bueno, 868, 01506-000, São Paulo, SP, Brazil
[34] Institute for Astronomy, University of Hawaii, 2680 Woodlawn Drive, Honolulu, HI 96822, USA
[35] Indian Institute of Technology, Hyderabad, Kandi Telangana 502285 India
[36] Department of Physics, University of Michigan, Ann Arbor, MI 48109, USA
[37] Instituto de Física Teórica UAM/CSIC, Universidad Autónoma de Madrid, E-28049 Madrid, Spain
[38] Kavli Institute for Particle Astrophysics & Cosmology, P.O. Box 2450, Stanford University, Stanford, CA 94305, USA
[39] Department of Particle Physics and Astrophysics, Weizmann Institute of Science, Rehovot, 7610001, Israel
[40] Enrico Fermi Institute, Department of Physics, Department of Astronomy and Astrophysics, and Kavli Institute for Cosmological Physics, University of Chicago, Chicago, IL 60637, USA
[41] Columbia Astrophysics Laboratory, Columbia University, New York, NY 10027, USA
[42] Center for Computational Astrophysics, Flatiron Institute, 162 W. 5th Avenue, New York, NY 10011, USA
[43] Physics Department, University of Wisconsin−Madison, Madison, WI 53706, USA
[44] Max-Planck-Institut fur Astrophysik, Karl-Schwarzschild-Str 1, D-85748 Garching bei München, Germany
[45] Instituto de Astronomía y Ciencias Planetarias, Universidad de Atacama, Copayapu 485, Copiapó, Chile
[46] Departamento de Física, Centro de Ciências Naturais e Exatas, Universidade Federal de Santa Maria, 97105-900, Santa Maria, RS, Brazil
[47] Núcleo de Astronomía, Universidad Diego Portales, Av. Ejército 441, Santiago, Chile

[48] Departamento de Ciencias Fisicas, Universidad Andres Bello, Avda. Republica 252, Santiago, Chile
[49] Instituto de Astrofísica, Pontificia Universidad Católica de Chile, Casilla 306, Santiago 22, Chile
[50] Millennium Institute of Astrophysics (MAS), Nuncio Monseñor Sótero Sanz 100, Providencia, Santiago, Chile
[51] Department of Physics and Astronomy, Johns Hopkins University, 3400 North Charles Street, Baltimore, MD 21218, USA
[52] Space Telescope Science Institute, 3700 San Martin Drive, Baltimore, MD 21218, USA
[53] Austin Peay State University, Dept. Physics, Engineering and Astronomy, P.O. Box 4608, Clarksville, TN 37044, USA
[54] Mt Stromlo Observatory, The Research School of Astronomy and Astrophysics, Australian National University, Canberra, ACT 2601, Australia
[55] National Centre for the Public Awareness of Science, Australian National University, Canberra, ACT 2611, Australia
[56] The ARC Centre of Excellence for All-Sky Astrophysics in 3 Dimensions (ASTRO 3D), Australia
[57] Benedictine University, Department of Physics, 5700 College Road, Lisle, IL, 60532, USA
Received 2021 June 12; revised 2021 September 1; accepted 2021 September 2; published 2021 December 28

Abstract

We present optical follow-up imaging obtained with the Katzman Automatic Imaging Telescope, Las Cumbres Observatory Global Telescope Network, Nickel Telescope, Swope Telescope, and Thacher Telescope of the LIGO/Virgo gravitational wave (GW) signal from the neutron star–black hole (NSBH) merger GW190814. We searched the GW190814 localization region (19 $\deg^2$ for the 90th percentile best localization), covering a total of 51 $\deg^2$ and 94.6% of the two-dimensional localization region. Analyzing the properties of 189 transients that we consider as candidate counterparts to the NSBH merger, including their localizations, discovery times from merger, optical spectra, likely host galaxy redshifts, and photometric evolution, we conclude that none of these objects are likely to be associated with GW190814. Based on this finding, we consider the likely optical properties of an electromagnetic counterpart to GW190814, including possible kilonovae and short gamma-ray burst afterglows. Using the joint limits from our follow-up imaging, we conclude that a counterpart with an *r*-band decline rate of 0.68 mag day^{-1}, similar to the kilonova AT 2017gfo, could peak at an absolute magnitude of at most −17.8 mag (50% confidence). Our data are not constraining for "red" kilonovae and rule out "blue" kilonovae with $M > 0.5\,M_{\odot}$ (30% confidence). We strongly rule out all known types of short gamma-ray burst afterglows with viewing angles $<17^{\circ}$ assuming an initial jet opening angle of $\sim 5^{\circ}.2$ and explosion energies and circumburst densities similar to afterglows explored in the literature. Finally, we explore the possibility that GW190814 merged in the disk of an active galactic nucleus, of which we find four in the localization region, but we do not find any candidate counterparts among these sources.

Unified Astronomy Thesaurus concepts: Gravitational waves (678); Neutron stars (1108); Black holes (162)

Supporting material: machine-readable tables

1. Introduction

Neutron star (NS) and black hole (BH) mergers are among the strongest gravitational wave (GW) sources from 10 Hz to 10,000 Hz (Press & Thorne 1972; Thorne 1997) and the primary astrophysical sources detected by the Laser Interferometer Gravitational Wave Observatory (LIGO) and Virgo collaboration (LVC; LIGO Scientific Collaboration et al. 2015; Abbott et al. 2017a). Although electromagnetic (EM) follow-up observations of these events began with the first detection of a binary black hole (BBH) merger by LIGO (Abbott et al. 2016a), it was not until the discovery of the binary neutron star merger (BNS) GW170817 that EM and GW emission was observed from the same source (Abbott et al. 2017b). GW170817 was accompanied by a prompt, short gamma-ray burst viewed off-axis (sGRB; Savchenko et al. 2017; Abbott et al. 2017c)[59] and later a kilonova called AT 2017gfo[60] discovered at optical wavelengths (Coulter et al. 2017). Follow-up observations of this event spanned the EM spectrum, and combined with the GW data these observations enabled unique insight into the nature of its ejecta (e.g., Cowperthwaite et al. 2017; Drout et al. 2017; Kasliwal et al. 2017; Kilpatrick et al. 2017; Smartt et al. 2017; Arcavi et al. 2017a), the engines that power sGRBs (Fong et al. 2017; Savchenko et al. 2017; Abbott et al. 2017c; Murguia-Berthier et al. 2021), and the NS equation of state (Radice et al. 2018; Abbott et al. 2018a).

The precise localization of GW170817 required coordination between the LVC and optical search teams (Coulter et al. 2017; Abbott et al. 2016b). Critically, all three LVC detectors contributed to the localization of GW170817 and the distance to this event was only ∼40 Mpc from the initial LVC analysis (Abbott et al. 2016b). This enabled a search of a relatively small volume of space that targeted galaxies in highly complete catalogs. Indeed, the greatest limiting factors in the speed with which AT 2017gfo was identified were the timescale required to generate accurate localization maps and the positioning of telescopes across the globe (Abbott et al. 2017b).

The same strategy has been less practical for all of the high-confidence NS mergers reported during LVC Observing Run 3 (O3; including GW190425, S190426c, GW190814, S190910d, S190910h, S190923y, S190930t, S191205ah, S191213g, and S200213t in Coughlin et al. 2019; Hosseinzadeh et al. 2019; Lundquist et al. 2019; Andreoni et al. 2019a; Dobie et al. 2019a; Gomez et al. 2019b; Goldstein et al. 2019c; Ackley et al. 2020; Andreoni et al. 2020; Antier et al. 2020; Morgan et al. 2020; Paterson et al. 2021; Pozanenko et al. 2020; Thakur et al. 2020; Vieira et al. 2020; Watson et al. 2020; Coughlin et al. 2020a; Alexander et al. 2021; de Wet et al. 2021). With greatly increased detector sensitivity and a higher rate of events detected at larger distances than GW170817, all LVC O3 events classified as NS mergers were less precisely localized than GW170817, with one exception. Given the rapid decline rates expected for EM counterparts (Roberts et al. 2011; Kasen et al. 2015), it is unlikely

[58] NASA Einstein Fellow.
[59] Although Kasliwal et al. (2017) argue this event was much weaker than sGRBs viewed at high redshift and likely the result of a shock breakout.
[60] Also called SSS17a, DLT17ck, and PS17egl.

that a counterpart would be detected. This is true even in the most optimistic counterpart models (Hosseinzadeh et al. 2019; Goldstein et al. 2019c; Andreoni et al. 2020; Morgan et al. 2020; Thakur et al. 2020; Alexander et al. 2021; de Wet et al. 2021), but especially after folding in realistic assumptions about the physical properties of NS mergers implied by GW data as in the case of GW190425 (Foley et al. 2020). Although some observations rule out AT 2017gfo–like counterparts over a large fraction of the localization regions of O3 events (e.g., Goldstein et al. 2019c; Morgan et al. 2020; Coughlin et al. 2020a), the total ejecta mass, composition, and merger properties of most NS mergers remain almost entirely unconstrained.

The need for better constraints is most pressing for GW events from neutron star–black hole (NSBH) and black hole–black hole (BBH) mergers where no viable EM counterparts have been confirmed (whereas GW170817 is widely considered to be the result of a BNS merger; Kilpatrick et al. 2017; Abbott et al. 2017b). Unlike BNS mergers where disruption of both NS components and some ejecta are guaranteed (Li & Paczyński 1998; Shibata & Taniguchi 2006; Metzger et al. 2010; Roberts et al. 2011), in an NSBH merger it is possible that the NS will eject no mass before it is entirely accreted by the BH. This is because the NS must be tidally shredded before it reaches the innermost stable circular orbit to produce ejecta, and whether this happens depends on the total mass of the system, the mass ratio, spins, and the radius (and thus the equation of state) of the NS (Faber et al. 2006; Lee & Ramirez-Ruiz 2007; Ferrari et al. 2010). Thus, for each new NSBH, the LVC infers the probability that mass remains outside the merger based on numerical-relativity simulations (i.e., `HasRemnant` in LIGO Scientific Collaboration & Virgo Collaboration 2019a, 2019b). Values reported by the LVC use an optimistic (stiff) equation of state, which maximizes the value of `HasRemnant` given constraints on the masses and spins of the merger components (Abbott et al. 2009). `HasRemnant` is often interpreted as the likelihood of seeing an EM counterpart similar to a kilonova or sGRB (Kasen et al. 2017; Troja et al. 2017). Beyond comparisons to relatively simple systems such as the GW170817 merger where ejecta are guaranteed, the validity of this estimate and the nature of EM emission from NSBH mergers have yet to be verified, and thus all `HasRemnant` estimates are subject to significant systematic uncertainties.

In the middle of O3 and roughly 2 yr after reporting GW170817, the LVC detected GW signal GW190814 on 2019 August 14 at 21:11:16 UT (LIGO Scientific Collaboration & Virgo Collaboration 2019a, 2019b; Abbott et al. 2020a). Detailed analysis indicated that this signal had high significance, implying a relatively close event with a low probability of a "false alarm" (with a rate of one per 10^{11} Hubble times that a spurious signal from correlated noise or detector "glitches" could produce GW190814; Singer & Price 2016). GW190814 was initially classified as a "Mass Gap" event with a primary BH and a secondary in the 3–5 $M_\odot$ range, but this classification was revised less than 12 hr later to an NSBH with high significance (i.e., with the secondary having a mass $<3\,M_\odot$ at $>99\%$ significance; Abbott et al. 2020a). In the final analysis of the GW190814 strain, the best-fitting template to the GW strain signal was the merger of $2.59 \pm 0.08\,M_\odot$ and $23.2^{+1.0}_{-0.9}\,M_\odot$ components at 235^{+40}_{-45} Mpc (Abbott et al. 2020a).

In addition to being the best-localized and one of the closest GW events to date, GW190814 had one of the most extreme mass ratios of all GW events detected during the LVC's first three observing runs. However, this analysis assumes that $2.59\,M_\odot$ NSs exist in nature, which may not be the case if the maximum-mass NS is below this threshold (Fattoyev et al. 2020; Tan et al. 2020; Godzieba et al. 2021; Kanakis-Pegios et al. 2021; Wu et al. 2021). The search for EM counterparts therefore provides unique insight into the nature of this threshold; detection of an EM counterpart from an NSBH merger with a massive secondary would imply that the maximum NS mass is at least as massive. Although analyses that classify GW190814 as an NSBH merger imply that the secondary is the most massive known NS, with significant implications for the compact binary population and their formation channels (Abbott et al. 2021a), it remains possible that GW190814 was a BBH system, incidentally making the secondary the least massive known BH.

The localization for GW190814 was rapidly refined to a localization region with size $\sim$38 deg^2 (90th percentile) on 2019 August 14 and centered approximately at $\alpha = 24.^\circ6$, $\delta = -24.^\circ8$ (J2000), although the final localization map presented by Abbott et al. (2020a) had a 90th percentile area of 19 deg^2 (Figure 1). Initial estimates of the `HasRemnant` statistic by the LVC was $<1\%$ (LIGO Scientific Collaboration & Virgo Collaboration 2019a), which is consistent with expectations that a $23.2\,M_\odot + 2.59\,M_\odot$ system would produce no ejecta even if the BH was maximally rotating. Significant EM follow-up observations of this event were triggered by several groups (Dobie et al. 2019a; Gomez et al. 2019b; Ackley et al. 2020; Andreoni et al. 2020; Vieira et al. 2020; Watson et al. 2020; Alexander et al. 2021; de Wet et al. 2021), which spanned gamma-ray through radio wavelengths and continued for >250 days after merger. No prompt gamma-ray signature was detected despite coverage of the localization region by INTEGRAL, Fermi, and Swift (Molkov et al. 2019; Kocevski et al. 2019; Palmer et al. 2019), and observations at X-ray through radio wavelengths did not reveal any likely counterparts.

Here, we present a joint analysis of the optical observations of the GW190814 localization region performed by the Gravity Collective, a collaboration consisting of follow-up efforts by the One-Meter Two-Hemisphere (1M2H) collaboration consisting of the Nickel, Swope, and Thacher telescopes, the Las Cumbres Observatory network, and the Katzman Automatic Imaging Telescope (KAIT) and representing imaging obtained on fourteen 0.7–1 m telescopes across the globe. We describe our optical searches and follow-up observations of candidates, including optical photometry and spectroscopy, in Section 2. In Section 3, we discuss our criteria for classifying candidates and conclude that no optical transients discovered from any source are likely counterparts to GW190814. None of our searches found a viable EM counterpart to GW190814, and so in Section 4 we place limits on the physical nature of any EM counterpart to GW190814. We compare our limits to models of a kilonova, an sGRB, and rapidly fading optical emission, from which we determine that our limits are not constraining for red kilonovae and we rule out blue kilonovae with an ejecta mass $>0.5\,M_\odot$ (30% confidence). We also rule out sGRB afterglows with viewing angles $<17^\circ$ (assuming a jet opening angle of $5.^\circ2$ as with GW170817 in Wu & MacFadyen 2018, 2019) and explosion energies and circumburst densities spanning the range presented by Fong et al. (2015). We conclude by discussing our overall search and follow-up strategy in Section 5 and the implications for discovering EM counterparts to GW events in future LVC Observing runs.

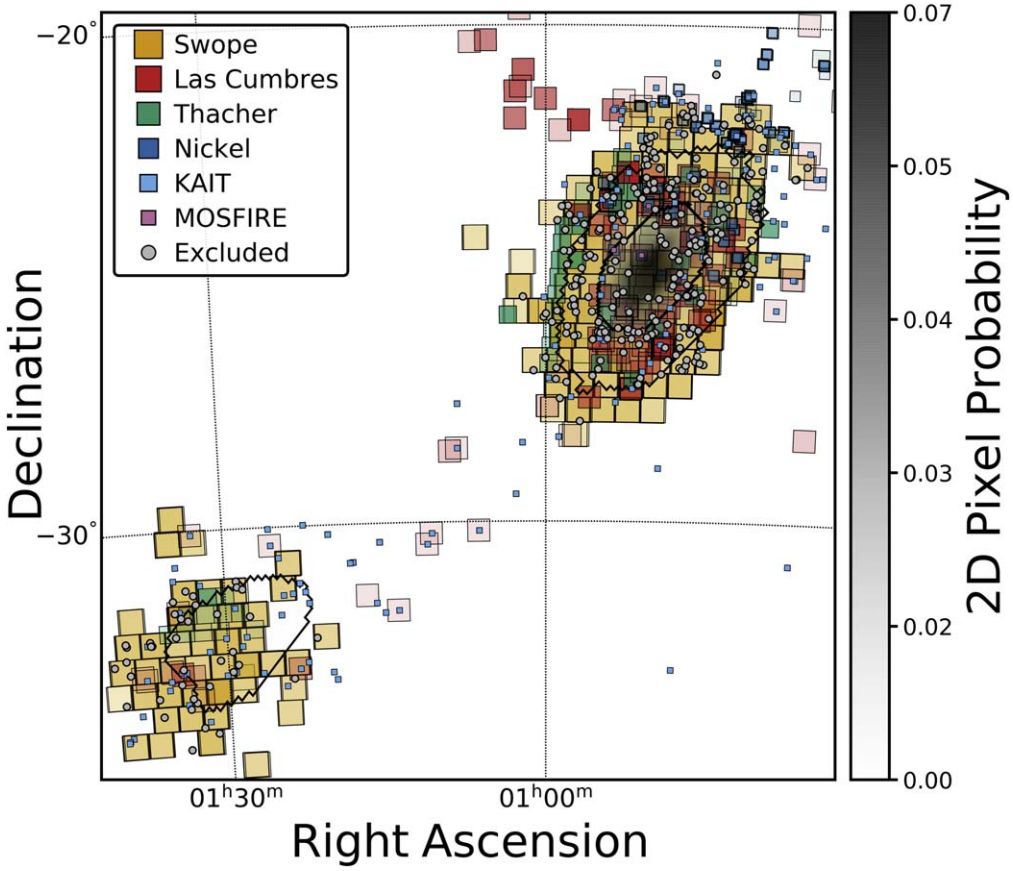

Figure 1. The LVC localization region of GW190814 (with contours at the 50th and 90th percentile localization) with our follow-up observations from KAIT (light blue), Las Cumbres (red), Nickel (dark blue), Swope (orange), and Thacher (green) overplotted. We also show candidate counterparts imaged near the GW190814 localization region and excluded candidates (gray).

All magnitudes presented in this paper are given in the AB system (Oke & Gunn 1983). Milky Way extinction is derived along the corresponding lines of sight from Schlafly & Finkbeiner (2011).

2. Observations

The 1M2H collaboration coordinated follow-up observations between three 0.7–1 m telescopes in order to search for optical counterparts to GW190814. The goal of this search and those involving the Las Cumbres Network and KAIT was to localize an optical counterpart to the gravitational wave event, which was known to resemble an NSBH merger (LIGO Scientific Collaboration & Virgo Collaboration 2019b). Based on NSBH merger models and their total ejecta masses (Faber et al. 2006; Ferrari et al. 2010; Rosswog et al. 2013), we inferred that likely counterparts would resemble a kilonova (likely redder than AT 2017gfo; e.g., see Metzger & Fernández 2014) or the afterglow from an sGRB. Based on the localization and luminosity distance to the event provided by the LVC and ultimately representing a volume of ∼39,000 Mpc^3 (Abbott et al. 2020a), our goal was therefore to localize a counterpart resembling one of these transients within the volume constrained by the event.

We prioritized 1M2H observations using the open-source code `teglon`,[61] which examines the LVC localization map and the GLADE galaxy catalog (Dálya et al. 2018) in order to optimally weight the priority of observing specific parts of the localization region over time. These observations were prioritized to maximize the likelihood of finding an EM counterpart under the assumption that it occurred in a galaxy in the LVC localization volume. In addition, we account for incompleteness in this catalog by weighting the priority of regions of sky without galaxies in the LVC volume by the corresponding LVC localization probability times the incompleteness integrated over the LVC localization volume. In this way, we account for situations in which the EM counterpart occurs in a galaxy not in any catalog. In total, we imaged 94% of the two-dimensional (2D) probability in the final LVC map of GW190814, as shown in Figure 1. We also prioritized some of our follow-up observations to image and obtain spectra of viable candidate counterparts as described below.

In addition, we coordinated observations with KAIT and 1 m telescopes in the Las Cumbres Network, all of which targeted galaxies (as in Arcavi et al. 2017b) in the localization region of GW190814. Finally, we observed eight galaxies and two counterparts in the localization region of GW190814 with Keck/MOSFIRE, although we were unable to obtain later follow-up imaging using the same instrument and filters. All observations are described below, and our follow-up images and candidate counterparts are shown relative to the final GW190814 localization region in Figure 1. The limiting magnitudes from these observations are shown in Figure 2 and compared with model light curves as well as those of AT 2017gfo.

[61] https://github.com/davecoulter/teglon

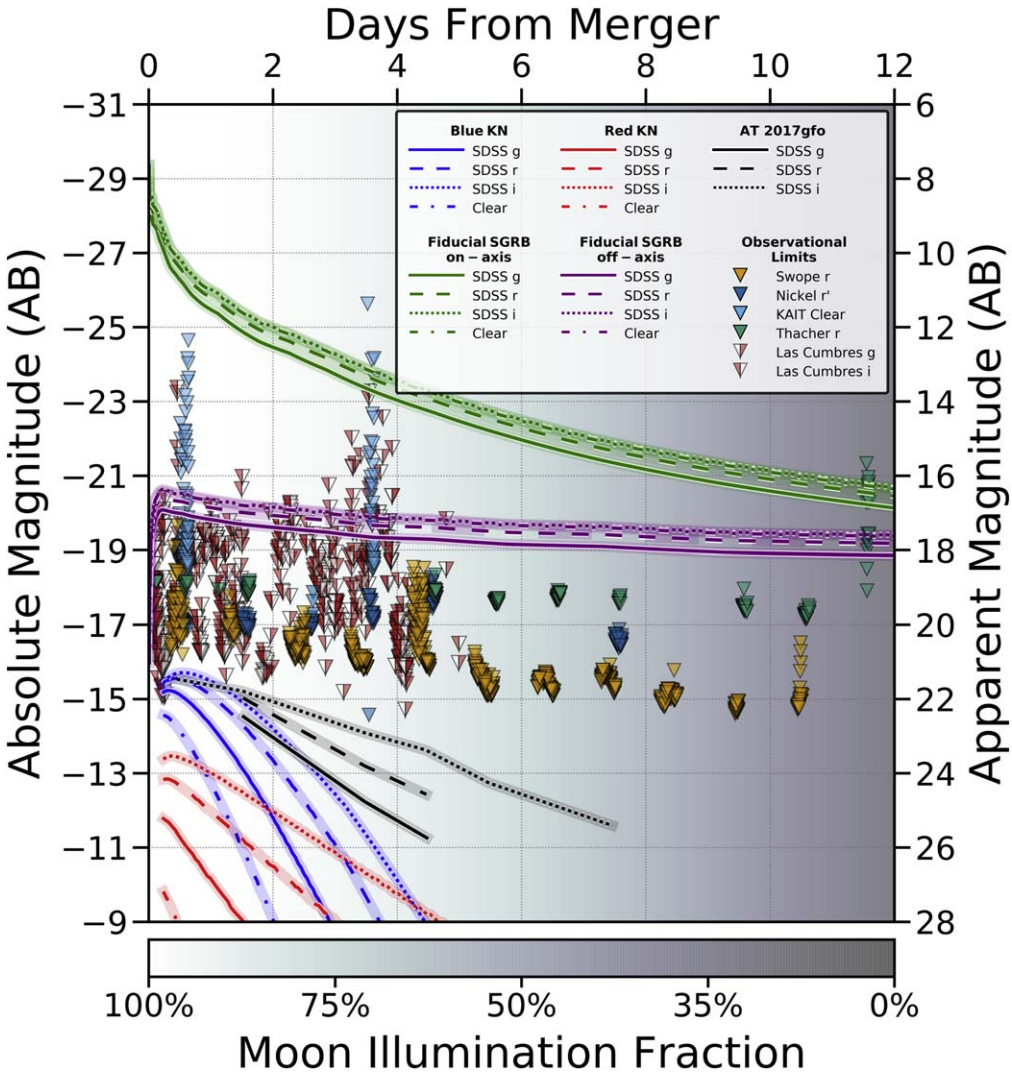

Figure 2. The limiting magnitudes from all of our follow-up observations of GW190814 with respect to the time from merger. We show the absolute magnitudes on the left-hand axis, based on the preferred distance to GW190814 of 241 Mpc, and apparent magnitudes on the right-hand axis. Each observation is colored by telescope and band as shown in the legend. We also overplot model light curves for the *gri* bands based on a blue kilonova with $M_{\rm ej} = 0.025\,M_{\odot}$, $v_{\rm ej} = 0.26c$, $Y_e = 0.45$, and also a red kilonova with $M_{\rm ej} = 0.059\,M_{\odot}$, $v_{\rm ej} = 0.19c$, $Y_e = 0.1$, which approximately represent the red and blue components of AT 2017gfo (see Section 4.2 and Drout et al. 2017; Kilpatrick et al. 2017). Similarly, we show GRB170817A viewed on-axis and off-axis at an angle of $\theta_{\rm obs} = 17°$ (Section 4.3 and Wu & MacFadyen 2018). Finally, we show smoothed *gri* light curves of AT 2017gfo derived from observations reported by Drout et al. (2017), Coulter et al. (2017), Arcavi et al. (2017a), Cowperthwaite et al. (2017), Troja et al. (2017), and Tanvir et al. (2017). We note that nearly all of our limits are below these light curves, and especially the yellow (Swope) and green (Thacher) limits that make up the majority of our pointings. To the extent that these two surveys cumulatively searched nearly the entire localization region of GW190814, the model light curves are ruled out approximately to 94% of the LVC two-dimensional probability we covered (Figure 1).

2.1. Imaging Search and Follow-up Observations

2.1.1. KAIT

The 0.76 m KAIT (Richmond et al. 1993; Filippenko et al. 2001) at Lick Observatory targeted galaxies in the localization region of GW190814 on 2019 August 15 and 18, as described by Vasylyev et al. (2019a, 2019b). Galaxies were selected from GLADE (Dálya et al. 2018) according to their *B*-band luminosity, with target priority reweighted by elevation at the time of observation. All observations were performed in a "Clear" filter. A total of 161 galaxies were targeted on 2019 August 15 with an additional 52 galaxies on 2019 August 18. All 213 fields were reimaged on 2019 August 24–25 to provide templates of the same fields for detailed analysis.

Following standard imaging and photometry procedures (e.g., Ganeshalingam et al. 2010; Zheng et al. 2017), the images were calibrated and point-spread function (PSF) photometry was performed using `DAOPHOT` (Stetson 1987) in `IDL`. The throughput of the KAIT "Clear" filter is known to be close to the *R* band (Li et al. 2003), so local AAVSO Photometric All-Sky Survey (APASS) standards (Henden et al. 2015)[62] were transformed to the Landolt *R* band (Landolt 1992) following Jester et al. (2005). Template images were then subtracted from the August 15 and 18 epochs using a custom `IDL`-based image-subtraction pipeline for PSF convolution. Finally, the limiting magnitude was estimated in each subtracted image by examining the 3σ rms noise within an aperture fixed to the size of the convolved PSF. These limits are provided in Table 1 with a median limiting magnitude of 18.2 mag.

[62] https://www.aavso.org/apass

Table 1
Optical/IR Imaging of the GW190814 Localization Region

Source[a]	α (J2000)	δ (J2000)	Date (MJD)	Filter	Magnitude Limit[b] (3σ)
S	01:27:55.560	−34:41:50.280	58,715.2170	*r*	20.64
S	01:27:56.496	−34:42:01.800	58,716.3976	*r*	21.04
S	01:27:58.248	−34:42:09.360	58,718.3350	*r*	21.12
S	01:27:46.752	−34:42:55.080	58,736.1369	*r*	20.69
S	01:32:06.792	−34:12:16.560	58,713.2037	*r*	20.37
S	01:32:07.752	−34:13:05.520	58,714.2115	*r*	19.58
S	01:32:09.456	−34:11:59.640	58,715.3197	*r*	21.03
S	01:32:12.288	−34:12:12.240	58,716.2327	*r*	20.73
S	01:32:08.400	−34:12:25.200	58,718.3299	*r*	21.04
S	01:32:06.096	−34:12:53.280	58,733.3072	*r*	20.84

Notes.
[a] Surveys correspond to KAIT (K), Keck/MOSFIRE (M), Las Cumbres Observatory (L), Nickel (N), Swope (S), and Thacher (T) imaging as described in Section 2.
[b] In-band 3σ limit for the reported image as described in Section 2 and Section 4. The "Clear" filter is abbreviated as "C" for all KAIT observations. All magnitudes are on the AB system (Oke & Gunn 1983).

(This table is available in its entirety in machine-readable form.)

2.1.2. Keck/MOSFIRE

We targeted 10 fields in a single epoch of target-of-opportunity imaging with the Multi-Object Spectrometer for Infra-Red Exploration (MOSFIRE; McLean et al. 2012) on the Keck I 10 m telescope on 2019 August 15 as shown in Table 1 and described by Brown et al. (2019). Two of these fields targeted candidates within the highest probability regions of GW190814; we observed AT 2019nmd and AT 2019nme (discovered by DESGW; Soares-Santos et al. 2019a; Morgan et al. 2020), both of which were undetected and later ruled out as likely minor planets (see Table 2). The remaining eight fields targeted galaxies within the inner 50th percentile localization region of GW190814. The final image mosaics consist of $6\farcm1 \times 6\farcm1$ frames centered on the coordinates reported in Table 1. All observations consisted of an eight-point dither pattern with 30 s of cumulative exposure time in the *J* band.

We reduced these data following standard procedures in the MOSFIRE data reduction pipeline[63] (e.g., Barro et al. 2014). The images were corrected for dark current and flat-fielded using calibration exposures obtained in the same instrumental configuration. We then obtained photometry of sources in each image using `DoPhot` and compared these sources to their *J*-band magnitudes in the 2MASS catalog (Cutri et al. 2003) to calibrate our images. Comparing to premerger 2MASS images of the same fields, we did not detect any transient sources in any of the Keck/MOSFIRE images (as reported by Brown et al. 2019).

The limiting magnitudes reported in Table 1 represent the average rms sky background inside a single PSF aperture, so they should not be interpreted as the limiting magnitude for any transient sources in our images. As we were unable to obtain template exposures for these fields, we do not include the Keck/MOSFIRE limits in the analysis of our constraints on EM counterparts to GW190814.

2.1.3. Las Cumbres

We also observed the localization region of GW190814 with the Las Cumbres Observatory global network (Brown et al. 2013), specifically with its 1 m telescopes at the McDonald Observatory in Texas, the Cerro Tololo Inter-American Observatory in Chile, the Siding Spring Observatory in Australia, and the South African Astronomical Observatory. Our pointings were selected based on the galaxy-targeted search and prioritization strategy outlined by Arcavi et al. (2017b). We obtained 300 s exposures in the *g* and *i* bands using the Sinistro cameras mounted on these telescopes, which have a $26' \times 26'$ field of view. Our initial results were reported by Hiramatsu et al. (2019b). Image processing was performed by the Las Cumbres Observatory BANZAI pipeline (McCully et al. 2018) and limiting magnitudes were extracted using `LCOGTSNpipe` (Valenti et al. 2016). We used Sloan Digital Sky Survey (SDSS), PS1, or DECam reference images in the appropriate bands to perform image subtraction using PyZOGY (Zackay et al. 2016; Guevel & Hosseinzadeh 2017). The limiting magnitudes were calculated by first estimating the Poisson noise due to the sky using the median absolute deviation of the entire image. Combining the Poisson and read noise, we estimate the 3σ limiting magnitude by inverting the standard signal-to-noise equation. The observations are summarized in Table 1 with a median limiting magnitude of 19.5 mag.

2.1.4. Nickel

We used the Nickel 1 m telescope at Lick Observatory, Mt. Hamilton, California, in conjunction with the Direct $2k \times 2k$ camera ($6\farcm8 \times 6\farcm8$) to observe galaxies in the localization region of GW190814 on 2019 August 14–19, 22, 27, and 30, as well as on 2019 September 3 and 11 (Table 1). These images were all obtained in the *r* band with 180 s exposures. Bias-subtraction and flat-fielding were done in `photpipe` (Rest et al. 2005) using calibration frames obtained on the same night and in the same instrumental configuration. We aligned our images using 2MASS astrometric standards in the image frame and calibrated the images with *r*-band standards obtained from the PS1 DR1 object catalog (Flewelling et al. 2020). Initial difference imaging was performed using `hotpants` with template images generated from the Dark Energy Camera (primarily DES DR1; Abbott et al. 2018b) and processed using the same pipeline, but our final difference-imaging analysis uses the exposures from September 3 and 11. In addition, we used a custom version of `DoPhot` (Schechter et al. 1993) to detect and perform forced photometry on all candidate

[63] https://keck-datareductionpipelines.github.io/MosfireDRP/

Table 2
Candidate Electromagnetic Counterparts to GW190814

Name	α (J2000)	δ (J2000)	Cumulative LVC Prob.[a]	Discovery Date (MJD)	Redshift[b]	Absolute Magnitude[c] (AB mag)	Note[d]
2019nmd	00:51:29.004	−22:28:16.96	0.9626	58,710.27800	⋯	⋯	(MP) 2010 GA33
2019nme	00:50:32.558	−22:13:33.70	0.9723	58,710.27800	⋯	⋯	(MP) 2005 OL33
2019noq	00:48:47.882	−25:18:23.46	0.3030	58,710.58500	0.05907 ± 0.00033 (s)	$i = -17.28 \pm 0.25$ (0.7 day)	(SN) II
2019nor	00:49:51.992	−24:16:17.71	0.1808	58,710.58500	0.43652 ± 0.00015 (s)	$r = -22.33 \pm 0.23$ (0.7 day)	(Z)
2019npd	00:46:56.705	−25:22:36.66	0.5377	58,710.28000	0.00081 ± 0.00001 (s)	$i = -8.68 \pm 0.30$ (0.4 day)	(Z; Sculptor Galaxy)
2019npe	00:41:33.330	−23:44:31.94	0.8787	58,710.27600	0.17233 ± 0.02355 (PS1)	$z = -19.55 \pm 0.30$ (0.4 day)	(Z)
2019npf	00:44:25.379	−23:11:52.08	0.7192	58,710.27600	0.17953 ± 0.02702 (PS1)	$z = -20.28 \pm 0.30$ (0.4 day)	(Z)
2019nph	00:58:07.613	−27:12:20.27	0.9362	58,710.30899	0.23849 ± 0.06683 (PS1)	$r = -20.88 \pm 0.30$ (0.4 day)	(Z)
2019npk	00:45:15.389	−20:58:23.75	0.9855	58,710.30600	⋯	⋯	(MP) 2015 XV140
2019npl	00:42:07.934	−21:57:09.23	0.9515	58,710.30500	⋯	⋯	(MP) 2014 VF30

Notes.
[a] Cumulative probability within the `GW190814_skymap` map provided by Abbott et al. (2020a).
[b] Redshifts are identified as spectroscopic (s) or photometric (by source) as described in Section 3.
[c] We indicate absolute magnitude at the earliest detection epoch (given in parentheses in observer-frame days relative to the GW190814 merger).
[d] We rule out each source based on classification as likely minor planets (MP), supernovae (SN), premerger variability (VAR), a redshift inconsistent with the GW190814 volume (Z), or photometric evolution (PHOT) as described in Section 3. For minor planets we give the identified minor planet, and for supernovae we give the type described in Section 3.2.
[e] The photometry used to rule out 2019qbz is presented in Ackley et al. (2020). Object 2019qbz has a relatively flat light curve across ≈6 days of follow-up as shown in Figure 5.

(This table is available in its entirety in machine-readable form.)

transient sources. The median limiting magnitude from our Nickel imaging is 19.8 mag.

2.1.5. Swope

We observed the localization region of GW190814 with the Swope 1 m telescope at Las Campanas Observatory, Chile, from 2019 August 14 to September 10 (Kilpatrick et al. 2019). Each observation is summarized in Table 1. The Swope/Direct 4k × 4k camera on the Swope telescope covers 29.′8 × 29.′7. We performed all observations in the *r* band with 120 s exposures. Bias-subtraction, flat-fielding, amplifier stitching, image registration, and calibration were all done in `photpipe` following methods described by Kilpatrick et al. (2018). We calibrated each image using *r*-band photometry of stars in the PS1 DR1 object catalog transformed to the Swope natural system using the Supercal method (Scolnic et al. 2015). We performed the difference-imaging procedure described in Section 2.1.4, and our final analysis uses template exposures obtained from 2019 September 2–8 and listed in Table 1. The median limiting magnitude from our Swope imaging is 20.6 mag.

2.1.6. Thacher

The Thacher 0.7 m telescope is a robotic telescope located at the Thacher School Observatory in Ojai, California, as described in Swift & Vyhnal (2018) and J. Swift et al. (in preparation). It uses an Andor iKON-L 936 2 k × 2 k imager with a *V*-band optimized back-illuminated chip that translates to a 20.′8 × 20.′8 field. We observed the localization region of GW190814 from 2019 August 15 to September 2 with 180 s *r*-band exposures (Swift et al. 2019). We followed the same calibration and reduction procedure in `photpipe` as described in Section 2.1.4. Each frame was calibrated using PS1 DR1 *r*-band standard stars, and we performed initial difference imaging using DECam frames and the final analysis with Thacher imaging templates of each field and described in Table 1. The median limiting magnitude from our Thacher imaging is 19.5 mag.

2.2. Spectroscopy of Candidates and Hosts

We obtained spectra of candidate EM counterparts to GW190814 and potential host galaxies with Keck, the Shane 3 m telescope at Lick Observatory, and the SOAR 4 m telescope on Cerro Pachón, Chile.[64] Obtaining optical spectra of candidate EM counterparts to GW events can validate whether these sources resemble expectations for kilonovae and sGRB afterglows, as in the case of the initial spectrum of AT 2017gfo obtained ∼12 hr after the GW event (Drout et al. 2017; Shappee et al. 2017). Similarly, optical spectra of transients unlikely to be associated with a GW event, such as supernovae, can be used to rule out a candidate counterpart. Finally, spectra provide a redshift to the event, enabling us to rule out candidate counterparts based on a volumetric cut in the context of the LVC localization region and luminosity distance. All of our spectroscopic observations are summarized in Table 3. Below we detail our observation and reduction procedure for each telescope.

[64] All spectroscopic data and analysis products are available at https://github.com/charliekilpatrick/gw190814.

2.3. Keck/DEIMOS

We obtained a spectrum of the GW190814 counterpart candidate AT 2019osy on 2019 August 28 using the DEep Imaging Multi-Object Spectrograph (DEIMOS; Faber et al. 2003) on the Keck II 10 m telescope. Two 900 s exposures were taken with a 1″ long slit, 600ZD grating, and the GG455 long-pass order blocking filter.

The spectra were reduced with the `PypeIt` version 1.3.3 (Prochaska et al. 2020a, 2020b) with the standard reduction. `PypeIt` was also used to flux calibrate the spectra with a standard star observed on the same night and to coadd the observations into a single spectrum.

2.3.1. Keck/MOSFIRE

We used Keck/MOSFIRE to observe the candidate counterpart to GW190814 AT 2019nrm on 2019 August 18 as reported by Dimitriadis et al. (2019). We obtained 4 × 120 s (ABBA nod pattern) *J*-band (∼11500–13500 Å) spectroscopic observations using the 0.″7 slit. The spectra were reduced with the MOSPY Data Reduction Pipeline[65] and calibrated with standard-star observations taken on the same night and in the same instrumental configuration. The final spectrum is shown in Figure 3.

2.3.2. Lick Shane/Kast

We observed candidate EM counterparts and host galaxies with the Kast double spectrograph (Miller & Stone 1993) on the Shane 3 m telescope on 2019 August 26 and 31, September 2, 5, and 21, and October 8 as shown in Table 3. All observations were taken with the 452/3306 grism (blue arm) and the 300/7500 grating (red arm), using the 2″ wide slit, covering approximately 3200–10500 Å in the combined blue-side and red-side spectra. The spectra were reduced with standard `IRAF`[66] CCD-processing and spectrum-extraction procedures, and our own `IDL` routines for flux calibration and telluric-line removal, using the well-exposed continua of spectrophotometric standard stars. Details on the spectroscopic reduction procedure are outlined by Silverman et al. (2012).

2.3.3. SOAR/Goodman

We used the Goodman spectrograph on the Southern Astrophysical Research (SOAR) 4 m telescope to observe candidate EM counterparts and host galaxies of GW190814 on 2019 August 17 and September 1. All observations were performed using the 400 line mm^{-1} M1 (3000–7000 Å) grating in conjunction with the 1.″07 wide slit. We reduced all spectra following the same procedures as for the Shane/Kast data. These spectra are shown in Figure 4 and discussed in Section 3.

2.4. Identification of Transients

Follow-up imaging from 1M2H, KAIT, and Las Cumbres was used to identify transients that we consider candidate counterparts to GW190814 after we performed difference imaging. Here, we summarize the methods used for elevating

[65] https://keck-datareductionpipelines.github.io/MosfireDRP/

[66] `IRAF` is distributed by the National Optical Astronomy Observatory, which is operated by the Association of Universities for Research in Astronomy (AURA), Inc., under a cooperative agreement with the National Science Foundation.

Table 3
Spectra of Candidates and Host Galaxies

Name	Observation Date	Source	Type	z	$z_{\rm phot,\ PS1}$	$z_{\rm phot,\ Legacy}$	Ref.
2019noq	2019-08-21	Goodman	II	0.0591 ± 0.0003	0.002 ± 0.078	0.050 ± 0.028	1,4
2019npf	2019-10-03	Kast	⋯	0.1630 ± 0.0001	0.180 ± 0.027	0.180 ± 0.022	2
2019nph	2019-10-31	Kast	⋯	0.2689 ± 0.0003[a]	0.238 ± 0.066	0.274 ± 0.049	2
2019npv[b]	2019-08-26	Magellan	Ibc	0.0560 ± 0.0001	0.071 ± 0.030	0.061 ± 0.054	1,3,4,11
2019npw	2019-08-27	Goodman	II	0.1494 ± 0.0001	0.197 ± 0.156	0.141 ± 0.054	3,5,6
2019nqc[b]	2019-08-23	SALT	II	0.0780 ± 0.0001	⋯	0.098 ± 0.065	1,4,5,7,11
2019nqg	2019-08-31	Kast	⋯	0.1706 ± 0.0001	0.147 ± 0.022	0.172 ± 0.020	5
2019nqq	2019-08-17	Goodman	II	0.0711 ± 0.0001	⋯	0.078 ± 0.016	1,4,8,11
2019nqr	2019-08-17	Goodman, FLOYDS	II	0.0832 ± 0.0001	⋯	0.046 ± 0.012	1,4,9,10,11
2019nqx	2019-10-08	Kast	⋯	0.2792 ± 0.0003[a]	0.265 ± 0.026	0.289 ± 0.010	12
2019nrd	2019-08-31	Kast	⋯	0.2472 ± 0.0003	0.250 ± 0.019	0.226 ± 0.007	12
2019nra	2019-09-21	Kast	⋯	0.2971 ± 0.0002[a]	0.269 ± 0.029	0.268 ± 0.022	12,13
2019nra	2019-08-18	MOSFIRE	?		0.269 ± 0.029	0.268 ± 0.022	12,13
2019nrb	2019-10-09	Kast	⋯	1.7953 ± 0.0011[a]	0.207 ± 0.027	0.203 ± 0.011	12
2019nrp	2019-11-06	Kast	⋯	0.0107 ± 0.0002[a]	⋯	0.255 ± 0.028	12
2019nrv	2019-10-09	Kast	⋯	0.0531 ± 0.0003[a]	⋯	0.060 ± 0.028	12
2019nte	2019-08-22	Goodman	⋯	0.0706 ± 0.0001	⋯	0.090 ± 0.020	4,11,14,15
2019nte	2019-10-08	Kast	⋯	0.0700 ± 0.0004[a]	⋯	0.090 ± 0.020	4,11,14,15
2019ntn	2019-08-21	Goodman	Ia-CSM	0.1001 ± 0.0002	⋯	0.318 ± 0.074	1,4,16
2019ntp	2019-09-01	Goodman	Ia	0.1141 ± 0.0001	0.229 ± 0.083	0.147 ± 0.020	1,4,15,16,17
2019ntr	2019-08-29	Goodman	II	0.2185 ± 0.0001	0.261 ± 0.245	0.193 ± 0.176	1,4,11,15,16,18
2019nts	2019-08-31	Kast	⋯	0.1931 ± 0.0003[a]	⋯	0.053 ± 0.181	1,16
2019nul	2019-08-31	Kast	⋯	0.0985 ± 0.0002	0.076 ± 0.030	0.095 ± 0.018	1,4,16,19
2019num	2019-08-27	Goodman	IIb	0.1274 ± 0.0001	0.129 ± 0.041	0.097 ± 0.017	1,4,15,16
2019nuo	2019-10-03	Kast	⋯	0.1151 ± 0.0001	0.089 ± 0.008	0.120 ± 0.019	15,19
2019nun	2019-09-05	Kast	⋯	0.1319 ± 0.0002	0.112 ± 0.023	0.113 ± 0.013	1,16,19
2019nur	2019-08-26	Kast	⋯	0.1394 ± 0.0002	0.127 ± 0.012	0.142 ± 0.026	16
2019nuu	2019-08-26	Kast	⋯	0.2106 ± 0.0002	0.204 ± 0.027	0.196 ± 0.022	16
2019nwt	2019-08-31	Kast	⋯	0.2458 ± 0.0003	0.210 ± 0.037	0.262 ± 0.027	20
2019nyv	2019-09-05	Kast	⋯	0.0410 ± 0.0004[a]	⋯	⋯	1,21
2019nyz	2019-08-26	Kast	⋯	0.4146 ± 0.0002	0.337 ± 0.057	0.018 ± 0.031	21
2019nzg	2019-08-26	Kast	⋯	0.2132 ± 0.0002	0.200 ± 0.023	0.223 ± 0.036	21
2019nzm	2019-09-21	Kast	⋯	0.2143 ± 0.0002	0.186 ± 0.015	0.025 ± 0.327	21
2019nzn	2019-09-03	Kast	⋯	0.1716 ± 0.0001	0.139 ± 0.036	0.161 ± 0.015	19,21
2019nzr	2019-09-02	Kast	⋯	0.2549 ± 0.0002	0.270 ± 0.041	0.255 ± 0.022	1,11,15,22
2019nzs	2019-10-03	Kast	⋯	0.2261 ± 0.0002	0.252 ± 0.027	0.234 ± 0.023	22
2019oat	2019-09-21	Kast	⋯	0.1978 ± 0.0003[a]	0.248 ± 0.119	0.195 ± 0.044	21
2019oaz	2019-09-03	Kast	⋯	0.1987 ± 0.0003	0.238 ± 0.032	0.222 ± 0.023	21
2019obb	2019-09-05	Kast	⋯	0.3157 ± 0.0002	0.335 ± 0.024	0.312 ± 0.008	22
2019obc[b]	2019-08-23	GTC	Ia	0.216 ± 0.005	⋯	0.276 ± 0.114	1,4,11,15,22,23
2019odc	2019-08-26	Kast	⋯	0.0551 ± 0.0002	0.049 ± 0.004	0.029 ± 0.015	1,4,11,15,24
2019ofb	2019-08-31	Kast	⋯	0.1185 ± 0.0001	0.184 ± 0.038	0.147 ± 0.028	1,25
2019omx	2019-08-29	Goodman	⋯	0.1645 ± 0.0001	⋯	0.214 ± 0.078	1,4,11,15,18,26
2019onj	2019-09-03	Kast	⋯	0.0665 ± 0.0001	⋯	⋯	1,11,15,27,28
2019osy	2019-08-28	DEIMOS	⋯	0.0738 ± 0.0003	⋯	0.098 ± 0.019	1,29,30,31

Notes. Our Keck/DEIMOS, Keck/MOSFIRE, Shane/Kast, and SOAR/Goodman spectra are described in Section 2.2. All dates are UTC. The spectral types for transient spectra are noted along with spectroscopic redshifts. We also note photometric redshifts from the two catalogs we use for our remaining candidates as an ad hoc check on the validity of these values. Where we have only measured the host galaxy redshift, we note the spectral type of the spectrum as "–." We provide references relevant to the discovery and classification of each candidate as follows: (1) Ackley et al. (2020), (2) Andreoni & Goldstein (2019a), (3) Gomez et al. (2019a), (4) Andreoni et al. (2020), (5) Andreoni & Goldstein (2019b), (6) Tucker et al. (2019a), (7) Buckley et al. (2019), (8) Herner (2019a), (9) Al (2019a), (10) Hiramatsu et al. (2019a), (11) Morgan et al. (2020), (12) Andreoni & Goldstein (2019c), (13) Dimitriadis et al. (2019), (14) Herner & Team (2019), (15) Soares-Santos et al. (2019b), (16) Andreoni & Goldstein (2019d), (17) Wiesner et al. (2019a), (18) Wiesner et al. (2019b), (19) Dobie et al. (2019b), (20) Al (2019b), (21) Andreoni & Goldstein (2019e), (22) Al (2019c), (23) Castro-Tirado et al. (2019), (24) Herner (2019b), (25) Chambers et al. (2019), (26) Al (2019d), (27) Al (2019e), (28) Japelj et al. (2019), (29) Jaodand et al. (2019), (30) Bauer et al. (2019), (31) Stewart et al. (2019b).

[a] Spectra did not meet our cross-correlation height-to-noise ratio (r) threshold $r > 4$. See discussion in Section 3.4.

[b] Spectra of these objects are not presented in this publication, but their classifications and redshifts are used in our analysis and can be found in the references given.

transient sources to candidate counterparts within each set of imaging. All photometry of transient sources used in this analysis, including photometry from outside sources (e.g., Ackley et al. 2020; Andreoni et al. 2020; Morgan et al. 2020), is summarized in Table 4.

2.4.1. 1M2H

As described above, all Nickel, Swope, and Thacher difference imaging was analyzed through the `photpipe` difference imaging and analysis pipeline. After difference imaging through `hotpants` and identification of transient sources using a custom version of

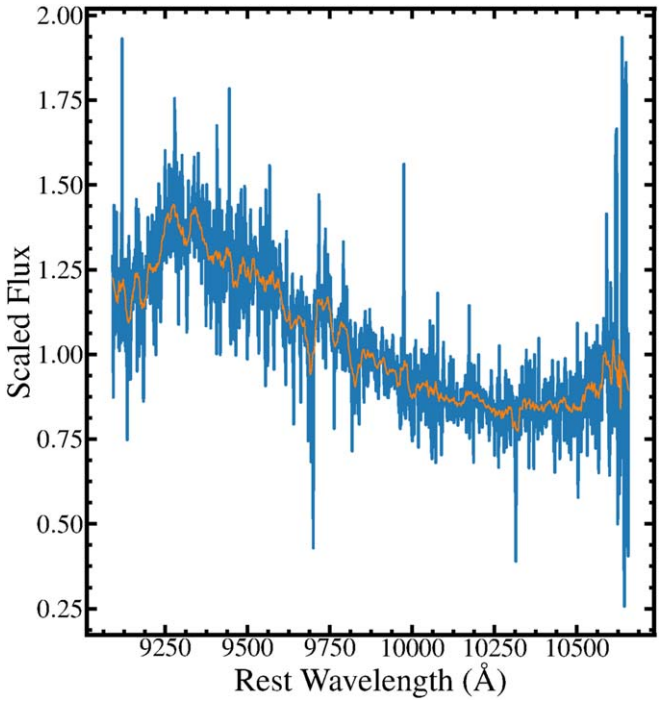

Figure 3. Keck/MOSIFRE spectrum of the GW190814 candidate counterpart AT 2019nra ($z = 0.269 \pm 0.029$) obtained on 2019 August 18 as reported by Dimitriadis et al. (2019). The spectrum is largely featureless apart from a single intermediate-width feature at a rest wavelength of 9300 Å, although this wavelength does not correspond to any known features.

dophot, photpipe cuts transient sources based on pixel-level statistics including the relative fraction of positive, negative, and masked (i.e., saturated) pixels within the PSF aperture and the extendedness of the source PSF relative to the PSF passed to dophot. In general, these criteria are relaxed in order to avoid cutting a significant fraction of the transient source catalog for each image, but these cuts naturally result in a loss in detection efficiency for each image (typically ∼3% of sources on average). We perform the same cuts during fake star injection, and so we account for this detection efficiency in our limiting magnitude for each image. On average, we detect 2 sources in each Nickel image, 12 sources in each Swope image, and 10 sources in each Thacher image.

After we construct a transient catalog for each image, sources are cross-matched across all catalogs using a search radius of 2 pixels; that is, transient sources within 2 pixels of the average coordinate of a previously identified "cluster" of detections are considered to be the same source. Sources are elevated as candidates if they are (1) detected in at least two images with a signal-to-noise ratio $S/N > 3$, or (2) in a single image with $S/N > 10$. We obtain final photometry for every cluster of sources by taking the signal-to-noise weighted average position of each cluster and running forced photometry on this position with dophot. Finally, we visually inspect all candidate transients to validate that they are not due to poor image quality or other nonastrophysical contaminants. All 1M2H candidates are cross-matched against known minor planets before we consider them as viable candidate counterparts to GW190814.

2.4.2. KAIT

KAIT images were analyzed through part of our custom-developed LOSSPhotPypeline[67] (Stahl et al. 2019), which adopts the ISIS package[68] (Alard & Lupton 1998) for image subtraction. After difference imaging, identification of transient sources was based on several parameters (e.g., PSF, FWHM, magnitude, and S/N) extracted from the original image, the template image, and the residual image using SExtractor[69] (Bertin & Arnouts 1996).

Candidates passing the customized criteria were logged on a web-based list and then further visually checked by multiple people to eliminate any nonastrophysical contaminants. Similar to 1M2H, all of our candidates were cross-matched against known minor planets before we considered them as viable candidate counterparts. If no valid candidate was found, the limiting magnitude was estimated by examining the 3σ rms noise averaged through several locations across the entire image.

2.5. Estimates of the Limiting Magnitudes

We estimate limiting magnitudes for Nickel, Swope, and Thacher difference images by planting artificial sources in each individual survey image, allowing us to determine the probability of finding a source as a function of magnitude. This procedure requires the following steps.

1. *Building the PSF model*: The PSF parameters for each image are determined by DoPhot (Schechter et al. 1993). We then rescale the PSF model such that the magnitude determined from the sum of the pixels in the model (given the predetermined zero-point of the image) is equal to the magnitude we wish to simulate.
2. *Planting the artificial sources*: For each image, we plant 1500 artificial sources in the regular, unsubtracted survey image. These sources are randomly placed across the image, with magnitudes randomly chosen from a flat distribution between 18 and 25 mag.
3. *Running the reduction pipeline*: Once the sources have been planted, we run the difference-imaging and source-detection pipeline with the exact same pipeline stages used for transient discovery, beginning at the difference image stage to incorporate correlated pixel noise and subtraction artifacts into the detection-efficiency calculation. We have verified that using 1500 sources does not adversely affect the quality of the difference images.
4. *Measuring the detection efficiency*: For bins of 0.2 mag, we compute the detection efficiency by dividing the fraction of sources detected in the difference image by the total number of simulated sources within that magnitude bin. This gives us the full detection efficiency as a function of magnitude, as well as the magnitude at which 50% of artificial sources are recovered. We define the 3σ limiting magnitude by interpolating our efficiency curves to the magnitude at which 99.7% of the average maximum fraction of recovered sources at any magnitude are at least as bright as that magnitude threshold. This fraction can be less than 100% if sources land on cosmic rays or on top of very bright stars, and we reweight our detection efficiency for that image by the maximum recovered fraction. These values correspond to the limiting magnitudes given for Nickel, Swope, and Thacher images in Table 1.

[67] https://github.com/benstahl92/LOSSPhotPypeline

[68] http://www2.iap.fr/users/alard/package.html

[69] https://github.com/astromatic/sextractor

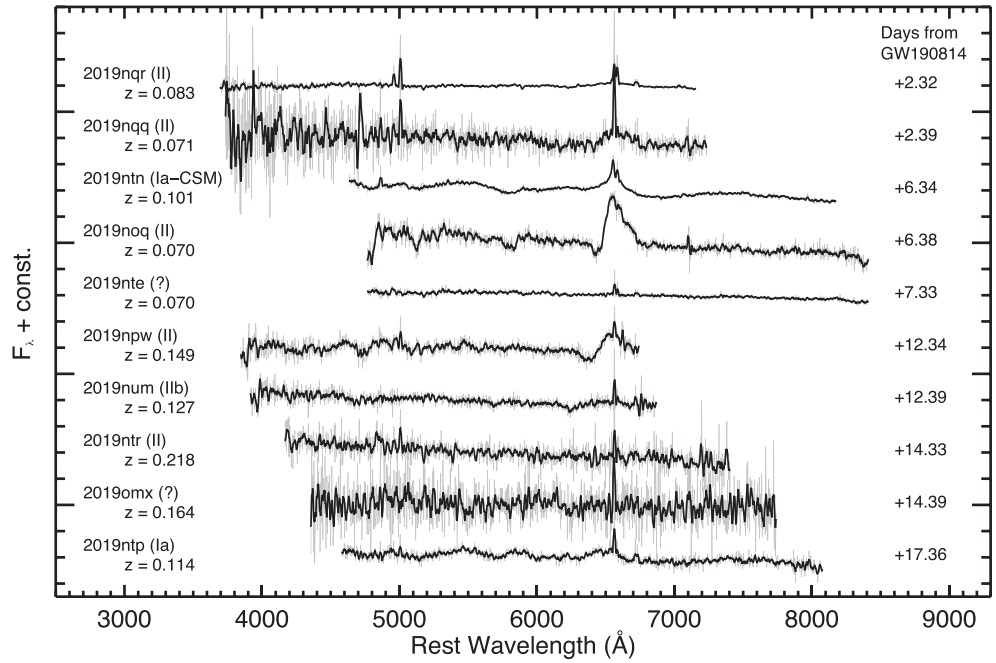

Figure 4. Spectra of candidate optical counterparts to GW190814 obtained with SOAR/Goodman. No spectra are classified as likely kilonovae or sGRBs, and thus we determine based on spectroscopic classification that most objects in this sample are unassociated with GW190814.

Table 4
Photometry of Candidate Electromagnetic Counterparts to GW190814

Name	MJD	Filter	m (mag)	σ_m (mag)	Source
2019noq	58,713.2883	*r*	20.12	0.10	Swope
2019noq	58,714.2699	*r*	20.39	0.10	Swope
2019noq	58,715.2022	*r*	20.44	0.09	Swope
2019noq	58,716.3051	*r*	20.46	0.06	Swope
2019noq	58,720.3270	*r*	20.42	0.04	Swope
2019noq	58,725.2115	*r*	20.42	0.04	Swope
2019noq	58,737.3559	*r*	20.57	0.08	Swope
2019npd	58,723.4640	*r*	19.67	0.11	Thacher
2019npd	58,734.1757	*r*	19.76	0.03	Swope
2019npe	58,713.2936	*r*	19.10	0.05	Swope

Note. All photometry of candidate counterparts (Table 2) to GW190814 from follow-up and search observations presented in this paper. We use these data along with photometry presented in Andreoni et al. (2020), Ackley et al. (2020), and Morgan et al. (2020) to classify all candidates.

(This table is available in its entirety in machine-readable form.)

These steps allow an "end-to-end" measurement of image-detection efficiency that includes correlated noise from the difference image convolution procedure and the ability of our automated software to recover point sources in our images. Correlated difference image noise in particular would not be measurable from a simple sky background based computation. These limits are also consistent with our cuts in transient identification, which are based on the same pipeline and identification process.

As discussed above, the limiting magnitude in KAIT and Las Cumbres images was estimated using the 3σ scatter in the background measured across each image.

2.6. Candidate Identification Compared with Other Searches

We consider the identification of candidates found in our search compared with those found in other surveys. In general, our search covered approximately the same area of sky as most other searches (e.g., Dobie et al. 2019a; Gomez et al. 2019b; Andreoni et al. 2020; Morgan et al. 2020; Thakur et al. 2020), with only a handful of our pointings targeted on galaxies well outside the 99% localization of GW190814, but much of our search reached at most ∼21 mag depth, covered times well past the first week after the merger was detected, and primarily occurred in the *r* band. Our search independently identified seven new candidates (2019aakm, 2019aakn, 2019aako, 2019aakp, 2019aakq, 2019aakr, and 2019aaks), which were entirely from our Swope and Thacher searches. These candidate detections all occurred >6 days from merger, and so mostly covered times when other searches had stopped.

For the remaining 182 candidates we consider in the analysis below, we identified 32 candidates, primarily from the Swope survey, which cumulatively identified 0.8 candidates $\deg^{-2}$. Similarly, Thacher identified 0.2 candidates $\deg^{-2}$ at a significantly shallower depth. The majority of these candidates were initially identified by DECam-GROWTH (24; Andreoni et al. 2020), with 6 identified by Pan-STARRS (Ackley et al. 2020) and the remaining 2 from the independent DECam analysis of Morgan et al. (2020). To the depth that these surveys achieved, we recovered 99% of all candidates that occurred in nearly contemporaneous imaging described here with depths greater than the discovery magnitude of that candidate. Similarly, the only candidates that we independently identified occurred in imaging after all but one epoch of DECam and Pan-STARRS observations (Ackley et al. 2020; Morgan et al. 2020), and so may have faded or not been flagged as a bona fide candidate in those searches.

All of the remaining 150 candidates are analyzed using a combination of our spectra, previously published data, and public data described below.

3. Classification of Candidates

Although no optical candidate counterparts to GW190814 were definitively identified as being similar to kilonovae or sGRBs in the extensive follow-up observations and analysis of the event (e.g., in the optical or radio; Dobie et al. 2019a; Gomez et al. 2019b; Andreoni et al. 2020; Morgan et al. 2020; Thakur et al. 2020), limits on the physical nature to any counterpart rely on the assumption that all transient sources identified in the aftermath of GW190814 have been ruled out as being associated with the GW detection. In the following analysis, we discuss all known candidate optical transients that we consider potentially associated with GW190814. We assess the likelihood that one of these transient sources was the EM counterpart to the merger using the localization region and time of merger, candidate spectroscopy, premerger variability, host-galaxy associations, and candidate photometry. The following criteria describe our classification procedure and rationale.

1. *Localization*: We consider publicly reported candidates and those discovered by our own surveys that are within the 99th percentile credible region provided by the LVC, a total area of 48.7 $\deg^2$ and 189 viable candidates (Figure 1). This can theoretically result in missing the actual counterpart, but we expect it to occur in only 1% of cases. Furthermore, we find that for the inner 95th percentile credible region (26.8 $\deg^2$) there are 214 viable candidates, while for the 99.5th percentile (58.2 $\deg^2$) there are 290 candidates. The fact that the number of candidates does not scale as the total search area reflects the shallower search depth of the lower-probability areas in the GW190814 localization region. Therefore, we are confident that we do not rule out any known, high-probability transients on the basis of localization.
2. *Time from merger*: We restrict our analysis to candidates discovered within 14 days after the LVC detected the GW190814 merger signal. This will only result in false negatives if the optical counterpart to GW190814 has a rise time significantly longer than known kilonovae and sGRBs such as AT 2017gfo (implying, for example, a kilonova with an extremely large ejecta mass and optical opacity or a highly off-axis GRB; Rossi et al. 2002; Yamazaki et al. 2003; Kasen et al. 2015; Ryan et al. 2015; Kasen et al. 2017; Metzger 2017). The lack of a prompt gamma-ray counterpart implies that if there was a GRB170817A-like GRB (Troja et al. 2017; Mooley et al. 2018), it was likely off-axis and thus not detectable by INTEGRAL, Fermi, or Swift (despite coverage of the region as described by Kocevski et al. 2019; Molkov et al. 2019; Palmer et al. 2019). However, while the rise time for a GRB afterglow scales relative to the viewing angle $\theta_{\rm obs}$ and jet opening angle θ_0 as $\theta_{\rm obs}/\theta_0$, optical follow-up observations would likely be insensitive to a counterpart observed >14 days after merger (see models by Lazzati et al. 2017; Murguia-Berthier et al. 2017). A delayed rise in optical luminosity could also occur if the merger occurred in an evacuated circumburst medium (proposed by Ramirez-Ruiz et al. 2019, for GW170817), similar to the Galactic pulsar J1913+1102 (Lazarus et al. 2016). However, for plausibly detectable EM counterpart models, the rise time is significantly shorter than 14 days, and so we are confident that this restriction is conservative. Furthermore, we find that if we restrict our analysis to candidates discovered only within the first 10 days post-merger while keeping our localization cut the same, there are 270 viable candidates, whereas if we cut at 21 days there are 293. Similar to localization, this reflects the fact that follow-up observations decreased significantly in depth and cadence at >10 days post-trigger. Criteria #1 and #2 define our initial sample of 189 candidate counterparts, including 7 candidates identified in our own follow-up program (Table 2).
3. *Coincidence with minor planets*: Candidates that are coincident (<20″) with minor planets at the time of observation and as reported by the Minor Planet Center,[70] and are not detected in multiple epochs of imaging separated by >30 minutes, are ruled out. For candidates discovered by 1M2H, KAIT, and Las Cumbres, we perform this check before considering a transient as a viable EM counterpart to GW190814, and so minor planets are not reported in Table 2. For all other publicly reported transients, this check is typically performed before a candidate is reported, but some reported candidates were reclassified as minor planets, for example, in Andreoni et al. (2020) and Morgan et al. (2020). Overall, we rule out 11 objects based on coincidence with minor planets.
4. *Coincidence with known stars*: We checked each candidate for coincidence (<1″) with nearby stars in the Gaia DR2 catalog (i.e., those that have a parallax or proper motion measured at >3σ; Gaia Collaboration et al. 2018). Transient detections can potentially arise from stellar variability, and so are not expected to be associated with GW190814. However, 0 objects are ruled out based solely on coincidence with Gaia DR2 stars.
5. *Spectroscopic classification*: Candidates with spectra that resemble known classes of transients (i.e., those with template spectra in SNID; Blondin & Tonry 2007) are ruled out as counterparts to GW190814. To perform this analysis, we consider spectra presented in publications on GW190814 (e.g., Andreoni et al. 2019a; Dobie et al. 2019a; Gomez et al. 2019b; Ackley et al. 2020; Watson et al. 2020, and references therein). We only consider spectra that we can definitively classify as supernovae or other well-known classes of transients that are not thought to be associated with NS mergers. For example, spectra that resemble "blue continuum" or galaxy emission are not ruled out, as AT 2017gfo was initially very blue (Drout et al. 2017; Kilpatrick et al. 2017; Shappee et al. 2017) and spectra dominated by galaxy emission imply nondetection of the transient. Thus, the likelihood of false negatives is negligible. We rule out 12 candidates based solely on spectroscopic classification, which includes all sources with classifications in Table 3.
6. *Premerger variability*: Candidates with detections in transient surveys from before the merger are ruled out, which we determine from cross-matching (<1″) to the Pan-STARRS DR2 Detection Catalog (see the description by Flewelling et al. 2020), an available light curve in

[70] https://minorplanetcenter.net

the ASAS-SN Photometry Database[71] (Shappee 2014; Jayasinghe et al. 2019), or the Asteroid Terrestrial-impact Last Alert System forced photometry server (Shingles et al. 2021). Models for merging NSBH systems do not typically predict any significant premerger optical emission, for example due to accretion from a circumbinary disk (Joss & Rappaport 1984; Schrøder et al. 2018); however, we further consider active galactic nucleus (AGN) variability (as in Graham et al. 2020) as a possible counterpart to GW190814 in Section 5.3. We define variability as multiple premerger detections in a single band with a significant ($>3\sigma$) change in brightness. We rule out 2 objects based solely on premerger variability, each of which is discussed below. We consider candidates ruled out by this criterion or any of the preceding steps to be "strongly ruled out" (as described in Table 2), comprising 114/189 (41%) of our sample.

7. *Spectroscopic redshifts*: The LVC constrain the distance to GW events using signal amplitude (Abadie et al. 2011). For GW190814, this resulted in a luminosity distance of 241^{+41}_{-45} Mpc ($z = 0.056 \pm 0.010$ assuming $H_0 = 70\,\mathrm{km\,s^{-1}\,Mpc^{-1}}$; Abbott et al. 2020a). Candidates found in host galaxies that are outside the 99th percentile credible volume (roughly $D_{\mathrm{mean}} \pm 2.58\,D_{\mathrm{std}}$) as determined from spectroscopic redshifts are ruled out. This criterion can result in false negatives when there is a chance coincidence between a candidate and assumed host galaxy. However, the mean number density of galaxies with luminosity $>L_\star$ in the local universe is approximately $6 \times 10^{-3}\,\mathrm{Mpc^{-3}}$ (Schechter 1976; Bell et al. 2003), implying roughly one galaxy per 85 arcmin^2. Where host identification is made, the median candidate-host separation is $\sim 2''$, and so the chance coincidence with a random host galaxy in the GW190814 volume is 0.004% (1 per 25,000 candidates), or a <1% chance of occurring at most once for all 189 of our candidates. To further reduce the likelihood of a chance coincidence, we require that for a galaxy with a spectroscopic or photometric redshift, the projected separation between the host galaxy and transient is <300 kpc (assuming Planck 2016 cosmology; Planck Collaboration et al. 2016). We derive spectroscopic redshifts from public databases, our own observations as described below, and observations in the literature. Therefore, we do not think that false negatives from candidates ruled out this way are significant. We rule out 33 candidates based solely on spectroscopic redshifts outside the 99% credible volume.
8. *Photometric redshifts*: We repeat the previous step using photometric redshifts from the 2MASS Photometric Redshift (2MPZ; Bilicki et al. 2014), Pan-STARRS1 Source Types and Redshifts with Machine learning (PS1-STRM) catalogs (Beck et al. 2021), and the Photometric Redshifts for the Legacy Surveys (Zhou et al. 2021). We choose the "best" host-galaxy association and photometric redshift by cross-matching galaxies between each catalog and picking the host galaxy with the smallest projected separation (in kpc), and then choosing the photometric redshift with the smallest relative uncertainty σ_z/z. All of these catalogs are trained using machine-learning approaches, and on 2MASS, Wide-field Infrared Survey Explorer (WISE), and SuperCOSMOS photometric data for the former and PS1 data for the latter. These result in median redshifts $z < 0.1$ for both catalogs, making them ideal for the low-redshift analysis of transients in the LVC volume. We rule out 102 candidates based on photometric redshift, representing 54% candidates overall.
9. *Photometric evolution*: It is now known that NS mergers result in kilonovae and sGRBs (Kasen et al. 2017; Abbott et al. 2017c), the optical properties of which have been constrained by sGRB follow-up observations at higher redshifts and the discovery of AT 2017gfo (Drout et al. 2017; Kilpatrick et al. 2017; Arcavi et al. 2017a). Apart from the most extreme physical scenarios and geometries, theoretical models and observations imply that EM counterparts to NS mergers are quite faint, fade rapidly, and typically have colors $g - r > -1.0$ mag (all "red" kilonova models considered by Kilpatrick et al. 2017 peak at >-18 mag, fade more rapidly than 0.1 mag day^{-1} in optical bands, and have $g - r > 1.0$ mag at all epochs). Therefore, we can rule out candidates that would be luminous at the distance to GW190814, have rising or slowly fading light curves, or are bluer than expected for sGRB afterglows. By using these limits and considering candidates with arbitrarily faint, rapidly evolving, or red light curves, we avoid false negatives due to host extinction. We rule out 28 candidates by photometric cuts, which represents all candidates not ruled out by previous cuts. Candidates ruled out only by these criteria are "weakly ruled out."

To systematically assess the viability of each candidate counterpart, we determine the extent to which all candidates match each of these criteria in Table 2. We start from our base sample of 189 candidates derived from publicly reported transients and candidates discovered in our follow-up imaging, all of which satisfy the localization criterion and were discovered in imaging taken within 2 weeks of the GW190814 merger. We conclude that there are no viable candidate counterparts, although 28 (14%) of all candidate counterparts are "weakly ruled out" by the photometric evolution criteria. In the remainder of this section, we discuss individual candidates and whether they are likely counterparts to GW190814 in the context of our overall classification scheme. We summarize the steps we use to rule out candidates in Table 5, including the number of candidates that can be ruled out at each step ignoring all previous steps.

3.1. Coincidence with Minor Planets

The primary interloping transients in our own follow-up imaging are minor planets, which result from asteroids with a proper motion that is high enough to appear in only a single epoch of imaging but low enough not to appear intrinsically extended in a 2–5 minutes exposure or show up in multiple exposures separated by <10 minutes. Andreoni et al. (2020) attempt to rule out these transients by taking multiple, nonconsecutive exposures when possible, but several objects in the Minor Planet Center database were reported when transients were detected only in a single epoch or the follow-up image occurred soon after discovery. In particular, we note the following transients in the Transient Name Sever that were reported with two detections but a short period of time between

[71] https://asas-sn.osu.edu/

Table 5
Analysis of Public and Internal Candidate Counterparts to GW190814

Step	Criterion	Candidates	Candidates Cut	All Candidates Flagged[a]
0	Within spatial (99th percentile area) and temporal cut (<2 weeks from merger)	189	…	…
1	Not <20″ from minor planet and not in multiple epochs separated by >30 minutes	178	11	11
2	Not <1″ from star with parallax in Gaia DR2	178	0	0
3	Not spectroscopically classified as an unassociated transient	166	12	12
4	No evidence for premerger variability	164	2	2
5	Spectroscopic redshift not outside the 99th percentile credible volume	133	33	39
6	Photometric redshift not outside the 99th percentile credible volume	28	102	127
7	Not photometrically classified as an unassociated transient	0	28	126

Note.
[a] This column indicates the number of candidates that would be cut at this stage if we disregard all previous stages.

the two epochs (given here in parentheses next to each candidate): AT 2019nmd (1.4 minutes), AT 2019nme (1.4 minutes), AT 2019nqh (single epoch), AT 2019nri (8.6 minutes), AT 2019nrq (2.9 minutes), AT 2019nrt (2.9 minutes), AT 2019nsd (2.9 minutes), AT 2019nsl (2.9 minutes), and AT 2019nsn (2.9 minutes); (Andreoni et al. 2019a; Morgan et al. 2020). In both Andreoni et al. (2019a) and Morgan et al. (2020), these candidates were subsequently revised to indicate that they are in fact minor planets as we note here.

Given the coincidence (<20″) between these transients and minor planets reported in Table 2 as well as the correlation with transients detected in a single epoch or at most two epochs separated by <30 minutes, we rule out all of these sources as likely minor planets and thus unassociated with GW190814. As described in Section 2.4, this cut was performed a priori for our own data, and so no internal candidates from 1M2H, KAIT, or Las Cumbres are considered likely minor planets.

3.2. Spectroscopy of Candidate Counterparts

Our Keck, Shane, and SOAR spectra of GW190814 candidate counterparts were obtained from 2019 August 17 to September 1 and definitively rule out some counterparts as being likely kilonovae or sGRB afterglows. Below we examine spectroscopic classifications of individual candidates inferred from spectra discussed in Section 2 and in other publications. Our classifications are performed using SNID (Blondin & Tonry 2007), from which we derive redshift and spectral type. All of our candidate spectra are shown in Figure 4.

AT 2019noq: We obtained a SOAR/Goodman spectrum of the candidate AT 2019noq (also PS19epf, discovered on 2019 August 15 by Huber et al. 2019) on 2019 August 21 as reported by Rodríguez et al. (2019). The spectrum is consistent with a Type II SN at $z = 0.07$, and so we do not consider AT 2019noq to be a likely counterpart to GW190814.

AT 2019ntn: AT 2019ntn was discovered on 2019 August 18 as part of DECam-GROWTH follow-up observations (Goldstein et al. 2019a, 2019b; Andreoni et al. 2020). We obtained a spectrum with SOAR/Goodman on 2019 August 21. This spectrum was reported as similar to that of a Type Ia-CSM or Ia/IIn at $z = 0.1$ by Rodríguez et al. (2019). We find similar results, and so we rule out any association between AT 2019ntn and GW190814.

AT 2019npw: AT 2019npw was initially reported by Andreoni et al. (2019b) at $i = 20.5$ mag and characterized as offset from its likely host galaxy. Tucker et al. (2019a) later obtained SOAR/Goodman spectroscopy of this source and found that it was consistent with a Type IIb SN at $z = 0.126$, which we confirm based on the same data. Therefore, we rule out any association between GW190814 and AT 2019npw.

AT 2019nqq: AT 2019nqq (also DESGW-190814c; Herner et al. 2019a) was discovered by the DESGW collaboration on 2019 August 15. We obtained a spectrum of this source on 2019 August 17 (Tucker et al. 2019b) that is dominated by a continuum with a broad emission line near 7000 Å. We infer this line to be Hα, implying that AT 2019nqq is consistent with a Type II SN at $z \approx 0.07$, similar to the results reported by Lopez-Cruz et al. (2019). Therefore, we rule out any association between AT 2019nqq and GW190814.

AT 2019nte: AT 2019nte was detected by Herner et al. (2019b) in DECam imaging at $i = 20.95$ mag on 2019 August 17. We obtained a spectrum of this source with SOAR/Goodman as reported by Cartier et al. (2019). It had too little signal to obtain a robust spectroscopic classification, but we obtained a redshift of the underlying host galaxy from the Balmer features. From this emission, we infer that AT 2019nte is at $z = 0.0701 \pm 0.0006$. At the location of AT 2019nte, this redshift is not ruled out by our volumetric cut, and so we consider AT 2019nte to be a viable candidate counterpart to GW190814 on the basis of its spectrum and redshift.

AT 2019ntp: The candidate AT 2019ntp was discovered by DECam/GROWTH (also DG19gcwjc; Goldstein et al. 2019b) on 2019 August 18 at $i = 21.0$ mag. We obtained a spectrum with SOAR/Goodman on 2019 September 1 as reported by Wiesner et al. (2019a); AT 2019ntp is a Type Ia SN at $z = 0.114$, and so we do not consider it to be associated with GW190814.

AT 2019ntr: Candidate transient AT 2019ntr was detected by DECam/GROWTH (also DG19sbzkc; Goldstein et al. 2019b) on 2019 August 18 at $z = 21.2$ mag. We obtained a SOAR/Goodman spectrum on 2019 August 29 (Wiesner et al. 2019b) from which we determine that AT 2019ntr is a Type II SN at $z = 0.218$. Therefore, we do not consider AT 2019ntr to be associated with GW190814.

AT 2019num:The candidate AT 2019num was discovered by DECam/GROWTH on 2019 August 18 at $i = 21.3$ mag (Goldstein et al. 2019b). We obtained a spectrum with SOAR/Goodman on 2019 August 27 (Tucker et al. 2019a) from which we determine that AT 2019num is a Type II SN at $z = 0.127$, and so it is not considered to be associated with GW190814.

AT 2019omx: The candidate AT 2019omx was discovered by the DESGW on 2019 August 21 at $z = 22.1$ mag (Soares-Santos et al. 2019b). We obtained a spectrum on 2019 August 29 with SOAR/Goodman (Wiesner et al. 2019b). The spectral

classification is inconclusive, although we are able to constrain the redshift from Balmer emission in the likely host galaxy as $z = 0.164$. Therefore, we rule out this candidate as being associated with GW190814 owing to its implied luminosity distance.

AT 2019osy: The GW190814 candidate EM counterpart AT 2019osy was discovered by the Australian Square Kilometre Array Pathfinder telescope (Johnston et al. 2007, 2008; McConnell et al. 2016) as a rising radio source possibly in host galaxy 2dFGRS TGS211Z177 ($z = 0.0738$) on 2019 August 23 and reported to the community on 2019 August 27 (Stewart et al. 2019a). We obtained a long slit Keck/DEIMOS spectrum of AT 2019osy and were unable to identify a transient. The extract spectrum is best matched by a galaxy template in SNID and we therefore determine that the transient is not detected.

3.3. Premerger Variability toward Candidate Counterparts

We analyzed the Pan-STARRS DR2 Detection catalog, ASAS-SN Photometry database, and Catalina Sky Survey DR2 catalog for coincidence with each of our candidates as described above. The PS1 DR2 Detection catalog separates multi-epoch observations into separate observations. We found two g-band detections coincident with AT 2019nto on 2010 September 8 with an aperture flux of $g = 20.08 \pm 0.02$ mag and on 2010 October 9 at $g = 21.56 \pm 0.05$ mag, indicating that the source is variable. It corresponds to the likely host galaxy WISEA J004203.40-244820.4 (Chung et al. 2011), with a nominal offset of $0\farcs28$ between AT 2019nto and the host galaxy. Therefore, we consider AT 2019nto to be unassociated with GW190814.

As described by Jayasinghe et al. (2019), the ASAS-SN photometry catalog was initially constructed from the >50 million point sources with $V < 17$ mag in the APASS catalog (Henden et al. 2015). Thus, sources with counterparts in the ASAS-SN catalog are not necessarily variable, but we can use the catalog to cross-match to candidate variables and check for multiple premerger detections. We identified a single candidate AT 2019nup that had a counterpart in the ASAS-SN photometry database.[72] This source is coincident with the center of a $z = 0.03665 \pm 0.00014$ galaxy in the Southern Abell Redshift Survey called SARS 013.16023-27.04103 (Way et al. 2005), with $0\farcs71$ between AT 2019nup and its host. The AT 2019nup premerger counterpart exhibited a previous outburst on 2016 May 15 at $V = 15.85$ mag, and so we rule out any association with GW190814.

Despite these findings, it is possible that AT 2019nto or AT 2019nup are associated with AGN activity as a result of a compact object merger (similar to Graham et al. 2020). We revisit these objects in Section 5.3.

3.4. Redshifts of Candidate Host Galaxies

We associate candidates with their likely host galaxies on the basis of projected separation from galaxies with spectroscopic redshifts in the NASA/IPAC Extragalactic Database (NED).[73] We require that the host-transient separation is at most $20'$ to be considered a candidate host galaxy and 300 kpc assuming the source is located at the host redshift and calculating an angular diameter distance using Planck Collaboration et al. (2016) cosmology. These criteria ensure that nearby extragalactic transients are selected in galaxies at large projected separations —notably AT 2019npd and AT 2019nvb, low-luminosity transients in the outer arms of the Sculptor Galaxy and separated by $9\farcm8$ (10.0 kpc) and $12\farcm6$ (12.7 kpc), respectively (Srivastav et al. 2019; Andreoni et al. 2019b). If there are multiple candidate host galaxies, we choose the galaxy with the smallest transient-host separation (in kpc). All of our host galaxy redshifts are noted in Table 2.

In addition, we measured redshifts to host galaxies of candidates without spectroscopic redshifts in NED with Shane/Kast and SOAR/Goodman (Table 3; note that two objects, AT 2019nra and AT 2019nte, in our table were observed twice and eight other objects have spectra that were too low quality to measure redshifts). From these spectra we infer the spectroscopic redshift to the candidate host galaxies. Spectroscopic redshifts were measured by cross-correlating spectra with galaxy templates using the RVSAO package (Kurtz & Mink 1998). In addition to visual inspection, the Tonry & Davis (1979) cross-correlation height-to-noise ratio (r) was used to determine the quality of the redshift match for each template, with $r > 4$ as our threshold for a reliable redshift.

The plurality of candidates we rule out are due to host-galaxy associations outside the 99th percentile volume provided by the LVC, totaling 33 with spectroscopic redshifts and 102 with photometric redshifts. Given the selection criteria and chance coincidence calculation described above, we infer that these associations are robust and it is unlikely that we have associated these transients with foreground or background galaxies outside the LVC volume by chance.

However, given the large overall fraction of galaxies with photometric redshifts and the statistical and systematic uncertainties associated with photometric redshift catalogs (see Bilicki et al. 2014; Beck et al. 2021; Zhou et al. 2021), it is possible that some host galaxies are indeed in the LVC volume. As a preliminary check, we consider the PS1-STRM and Legacy photometric redshifts of candidate host galaxies in Table 3 for which we have spectroscopic redshifts.

We also perform an additional check to avoid this possibility by requiring that, in order to be considered "outside the LVC volume," the photometric redshift $z_{\rm phot}$ and uncertainty $\sigma_{z_{\rm phot}}$ must satisfy $z_{\rm phot} + \sigma_{z_{\rm phot}} < z_{\rm LVC} - \sigma_{z_{\rm LVC}}$ or $z_{\rm phot} - \sigma_{z_{\rm phot}} > z_{\rm LVC} + \sigma_{z_{\rm LVC}}$ (where $z_{\rm LVC}$ and $\sigma_{z_{\rm LVC}}$ are the redshift and uncertainty implied by the luminosity distance from the LVC HEALPix map and assuming Planck Collaboration et al. 2016 cosmology). However, this would not necessarily rule out catastrophic outliers that were incorrectly classified in the PS1-STRM or Legacy method. As an ad hoc check on the validity of PS1-STRM and Legacy photometric redshifts, we analyzed the photometric redshifts for galaxies whose redshifts are measured spectroscopically in Table 3. Although there are some catastrophic outliers in both catalogs and at all redshifts (2019nqr, 2019nrd, 2019nrb, 2019nrp, 2019nuo, and 2019nyz at $>3\sigma$), we do not identify any instances where the spectroscopic redshift would place the host galaxy inside our fiducial GW190814 volume but the photometric redshift would not. In general, we consider both PS1-STRM and Legacy to be a reliable indicator for cases where the transient host galaxy is more distant than GW190814, which is the case for all candidate host galaxies we rule out by photometric redshift.

For analyses using GW190814 to measure the Hubble constant statistically (as by Soares-Santos et al. 2019c; Palmese et al. 2020; Vasylyev & Filippenko 2020; Abbott et al. 2021b),

[72] This source is called AP16326416 in the ASAS-SN Photometry Database.
[73] http://ned.ipac.caltech.edu/

additional spectroscopic observations of galaxies in the GW190814 volume will be essential to reduce the uncertainties in host-galaxy associations and the Hubble constant.

Some apparently "hostless" sGRB afterglows have been localized to regions of the sky with no apparent host galaxy to deep limits of $V \approx 26$ mag (Fong & Berger 2013; Behroozi et al. 2014). This finding suggests that some BNS and NSBH binaries experience natal kicks of $>150\,\mathrm{km\,s^{-1}}$ and potentially travel hundreds of kiloparsecs before merging and producing GW signals detectable by the LVC. This scenario is more likely in the local universe where merging NS systems are more heavily weighted toward long delay times and thus systems that have traveled further from their birth environments (Anand et al. 2018; Safarzadeh et al. 2019). We do not consider apparently hostless transients to be ruled out as candidate counterparts to GW190814, and so the primary effect of a large projected separation between a transient and host on our analysis is the increased probability of a chance coincidence. A more detailed analysis would marginalize over the likelihoods of all candidate host galaxies for all candidate counterparts (as in, e.g., Aggarwal et al. 2021) and only cut candidates if they are associated with a galaxy outside the localization volume with high probability.

3.5. Photometric Evolution of Candidates

To constrain the optical properties of each candidate, we assign them luminosity distances on the basis of redshift (where available in Table 2) or the luminosity distance at the transient location in the LVC GW190814 HEALPix map. Thus, we infer the absolute magnitude of every candidate that is not a minor planet in our analysis. Many of these sources are inferred to have extremely luminous absolute magnitudes (<-21 mag), likely reflecting interloping AGNs found in galaxy-targeted searches (e.g., Véron-Cetty & Véron 2010; Smith et al. 2020), and so most of these sources were ruled out on the basis of host-galaxy associations and our volume cut.

Guided by theoretical models for kilonovae, we note that there are no plausible models more luminous than -18.0 mag (e.g., in Kasen et al. 2017; Metzger 2017, 2019; Morgan et al. 2020), and thus use this limit to exclude any particularly luminous sources comprising 14 candidates. In addition, where available we analyzed any variability in all photometric bands and rule out sources that decline more slowly than $0.1\,\mathrm{mag\,day^{-1}}$ over a baseline of at least 3 days. We rule out six objects (AT 2019omw, AT 2019qbz, AT 2019zza, 2019aako, 2019aakp, and 2019aakq) as candidates that were either rising or slowly declining at the time of observation. In addition, we place limits on the nondetection of some candidates in images obtained before they were reported by other groups. Thus, we can place a limit on the decline or rise rate, depending on the relative depth of our nondetection compared to the discovery magnitude, assuming the source was fainter than the limit at the time of *our earlier* observation (in particular, for candidates reported by Andreoni et al. 2019a; Morgan et al. 2020). We rule out eight candidates based on this criterion. The light curves and limits for all candidates ruled out by photometric cuts are shown in Figure 5.

We acknowledge that these cuts are model dependent, and so the 28 candidates rejected at this stage remain viable if there is a potential NSBH EM counterpart model that matches any of the criteria on which we cut. In particular, we directly compare our empirical limits on the minimum absolute magnitude and decline rate (Section 4.4) to these candidates in order to highlight that our limits are consistent with sources discovered by our surveys and in the literature. However, our photometric constraints are the weakest criteria for ruling out candidate counterparts and only pertain to candidates that cannot be ruled out in any other context.

4. Limits on Electromagnetic Counterparts

Having determined that the candidate counterparts discussed above are not likely counterparts to GW190814, we consider the depth of each image as determined in Section 2.5 and shown for each pointing used in this analysis in Table 1. In the remainder of this section, we analyze these limits in the context of model optical counterparts to GW190814 and place constraints on the properties of any hypothetical counterpart.

4.1. Constraints on EM Counterparts to GW190814

We have demonstrated that there is no candidate counterpart to GW190814 in Section 3. In the following analysis, we determine the joint limits on the presence of an EM counterpart to GW190814 using all difference imaging (neglecting our template images and Keck/MOSFIRE images for which we do not have templates). In practice, this involves comparison between the expected in-band light curves for various transient sources and the 3σ limiting magnitudes as a function of sky position and time relative to merger reported in Table 1. In order to provide a physically meaningful limit, we emphasize that our uniform sample of difference images is reduced self-consistently with (1) template exposures of each targeted field obtained in the same filter and instrumental configuration, (2) true PSF-convolved difference imaging between all science exposures and the template exposures as described in Section 2, and (3) limiting magnitudes derived in the difference images themselves and consistent with the signal-to-noise ratio of any detected transient sources. In this way, we are confident that our limiting magnitudes rule out any EM counterparts across our imaging to the magnitude level quoted in Table 1. We emphasize that while our limiting magnitudes account for Milky Way extinction in the direction of each image, we assume there is no additional source of extinction, for example in the host galaxy or local environment of the GW190814 progenitor system.

We obtained the latest GW190814 HEALPix[74] (Górski et al. 2005) sky-localization map from the Gravitational-Wave Candidate Event Database[75] and presented by Abbott et al. (2020a). All observations and limiting magnitudes reported in Table 1 were then ingested into our GW planning and analysis code `teglon` (see Section 2) and cross-matched to the corresponding HEALPix pixel elements. At each pixel, we estimated the mean and standard deviation of the best-fitting LVC distance using the `moments_to_parameters` from the `ligo.skymap.distance` Python package (Singer et al. 2016a, 2016b). Each resulting Gaussian is then truncated at zero distance and renormalized such that the total three-dimensional probability (i.e., integrated over all sky pixels and luminosity distances) is unity.

We then consider the likelihood that an optical counterpart to GW190814 would be detected for a given counterpart model, which we generically classify as kilonovae (Section 4.2),

[74] http://healpix.sourceforge.net
[75] https://gracedb.ligo.org/

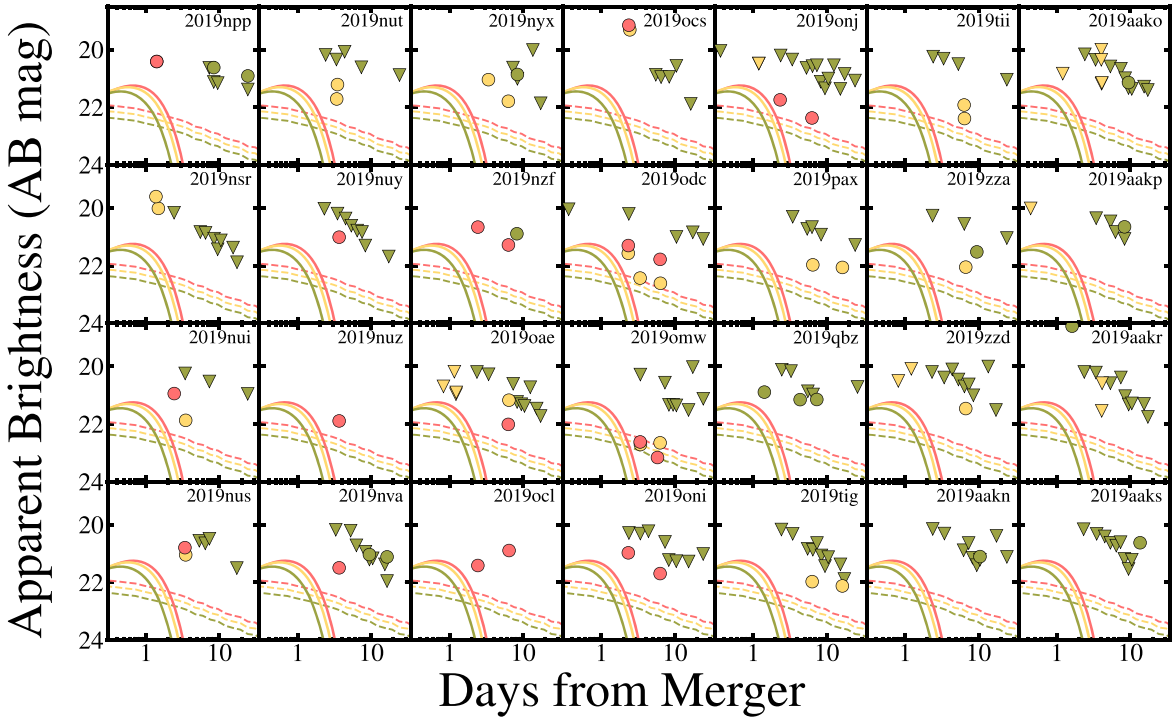

Figure 5. The *riz* (green, yellow, and red, respectively, with detections represented as circles and upper limits as triangles) light curves of candidate counterparts to GW190814 that we ruled out on the basis of photometric cuts as described in Section 3.5. We show photometry from our own follow-up (Table 4), DECam (Andreoni et al. 2019a; Morgan et al. 2020), and VLT-GRAWITA (Ackley et al. 2020) for each source that we rule out on the basis of light-curve parameters. For comparison, we show blue kilonova light curves (solid lines) and gamma-ray burst afterglow light curves corresponding to the off-axis GRB 170817A analog (dashed lines) corresponding to the models shown in Figure 2. We place each model light curve at the distance of each candidate using redshift information where available or the luminosity distance at its location in the GW190814 localization map (from Abbott et al. 2020a). In general, the detected candidates are significantly more luminous than the models we consider and at the observed epochs, which enable us to rule out these candidates as too luminous to be a counterpart to GW190814 in Table 5.

sGRBs (Section 4.3), and linearly evolving optical counterparts (Section 4.4). Each model provides an estimate of the brightness of the counterpart as a function of time, wavelength, and distance, which we transform to in-band light curves using `pysynphot`.

Over the GW190814 localization region, most areas were observed with multiple images and in multiple filters. Therefore, to compute the net detection efficiency given all sky map pixels and all observations, we determine the detection efficiency in a given model for each sky map pixel across each epoch and filter, and then combine the result into a cumulative detection efficiency. To do this, we retrieve the absolute magnitude for a given model at the time and in the band of each observation. Our inferred detection efficiency is also dependent on specific image- and line-of-sight dependent quantities, for example the Milky Way extinction and limiting magnitude as described in Section 2.5.

We then reparameterize our limiting magnitude in terms of the distance $D_{\mathrm{model}_{j,f}}$ at which we would expect to detect a source in image j with a filter f and a limiting magnitude $m_{j,f}$, where the source has an absolute magnitude $M_{\mathrm{model}_{j,f}}$ and line-of-sight extinction A_f, as

$$\mu_{\mathrm{model}_{j,f}} = m_{j,f} - M_{\mathrm{model}_{j,f}} - A_f \quad (1)$$

$$D_{\mathrm{model}_{j,f}}\,[\mathrm{Mpc}] = 10^{0.2\times(\mu_{\mathrm{model}_{j,f}}-25)}. \quad (2)$$

For each pixel i in the LVC localization map that overlaps with image j, we then calculate the relative efficiency of detecting this model by integrating the pixel distance distribution from zero distance to $D_{\mathrm{model}_{j,f}}$,

$$P_{\mathrm{model}_{i,j}} = \frac{1}{\sqrt{2\pi}\,\sigma_{D_i}} \int_0^{D_{\mathrm{model}_{j,f}}} e^{-\frac{1}{2}\left(\frac{\bar{D}_i - D}{\sigma_{D_i}}\right)} dD, \quad (3)$$

where $\bar{D}_i$ is the mean distance and σ_{D_i} is its standard deviation corresponding to the pixel i in the localization map.

To combine independent observations that overlap with each pixel, we take the complement of the joint probability that we do not see the source in any epoch. That is, for each pixel, we weight the relative likelihood that we would detect a specific model in image j by the LVC 2D pixel probability in each pixel $_{Pi}$ and sum over all pixels to obtain a cumulative probability of detecting a specific model,

$$P_{\mathrm{model}} = \sum_i P_i[1 - \prod_j (1 - P_{\mathrm{model}_{i,j}})]. \quad (4)$$

This final probability, which we interpret as the likelihood that we would have seen a source with properties described by a model for the EM counterpart to GW190814, is calculated for a wide range of models described below.

4.2. Limits on Kilonovae

The counterpart to GW170817 was initially localized by targeting optical emission from a kilonova (Coulter et al. 2017; Kasen et al. 2017; Abbott et al. 2016b), or a transient powered by the decay of *r*-process species synthesized in ejecta from an NS merger. As in Kilpatrick et al. (2017), we parameterize this source for a given ejecta mass m_{ej} and velocity v_{ej}. Following the numerical model presented by Metzger (2017) and used by

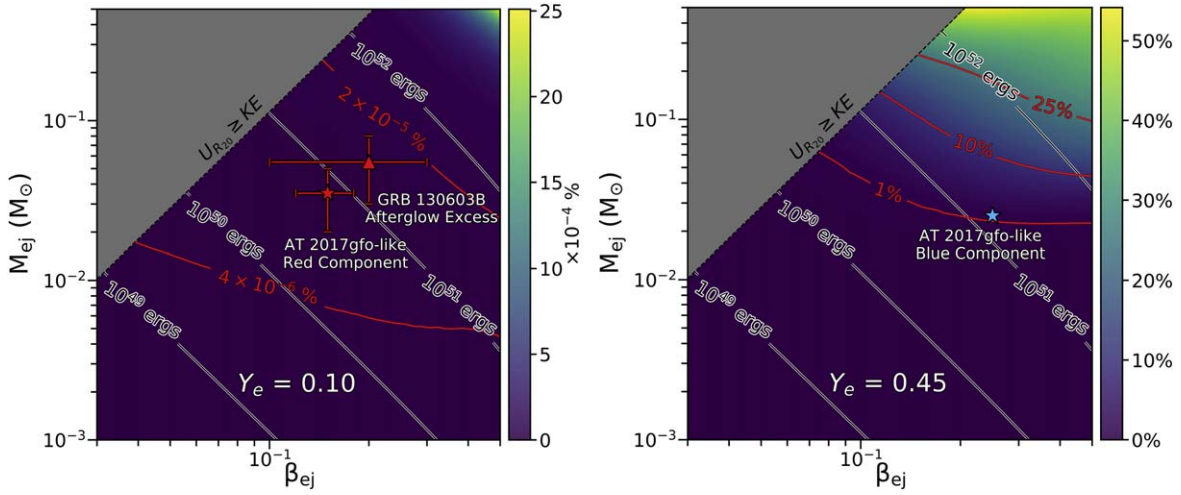

Figure 6. Constraints on the presence of a kilonova assuming an electron fraction corresponding to a "red" kilonova ($Y_e = 0.10$, left) and a "blue" kilonova ($Y_e = 0.45$, right). For both sets of models, we show the estimated likelihood that we would have detected a source for a given ejecta mass (m_{ej} in $M_\odot$) and velocity (β_{ej} in natural units) following the procedure in Section 4.1. We have grayed out the region where the binding energy of the ejecta (assuming an extremely stiff NS radius of 20 km) exceeds its kinetic energy. For context, we show contours of equal probability in red and lines of equivalent ejecta kinetic energy in black. Finally, in each panel we show the location of the corresponding kilonova ejecta component AT 2017gfo as derived by Kilpatrick et al. (2017; specifically $\beta_{ej} = 0.15$, $M_{ej} = 0.035\ M_\odot$ for the red kilonova and $\beta_{ej} = 0.25$, $M_{ej} = 0.025\ M_\odot$ for the blue kilonova) as well as the putative kilonova counterpart to GRB130603B as described by Tanvir et al. (2013).

Coughlin et al. (2019, 2020a), we allow for a varying electron fraction Y_e in the ejecta, which affects the neutronization and thus the composition of the ejecta. Broadly speaking, low electron fractions will lead to a high level of neutronization and thus heavier *r*-process species, which tend to be more optically thick at the optical and near-infrared wavelengths of our search. The electron fraction and distribution of *r*-process species have a secondary effect on the radioactive heating rate (e.g., see Lippuner & Roberts 2015), which is incorporated into our light curves, but the ejecta opacity is the dominant effect of varying Y_e.

In order to accurately estimate the ejecta opacity as a function of electron fraction, we adopt the mean opacity for kilonovae with varying compositions presented by Tanaka et al. (2020, see their Table 1) but with a floor of $\kappa = 1.0\,\mathrm{cm^2\,g^{-1}}$ for $Y_e > 0.40$. This results in relatively high opacities of $\kappa > 30.0\,\mathrm{cm^2\,g^{-1}}$ for $Y_e \lesssim 0.15$, and so this model is somewhat pessimistic compared with similar treatments by Andreoni et al. (2020) and Coughlin et al. (2020a). However, we are confident that our models accurately reflect a broad range of ejecta composition for varying masses and velocities.

We estimated the in-band light curves for ejecta masses 0.001–0.5 $M_\odot$ and velocities (0.001–0.5)*c*. We show our estimated probability of detection for our fiducial models, a "red" kilonova ($Y_e = 0.10$) and a "blue" kilonova ($Y_e = 0.45$), in Figure 6.

4.3. Limits on sGRBs

We adopted the models of Duffell & MacFadyen (2013) and Wu & MacFadyen (2018) to model potential sGRB optical counterparts to GW190814. We parameterize these models by the isotropic kinetic energy $E_{K,iso}$ and the circumburst density n as well as the viewing angle of the sGRB jet θ_{obs} (assuming a jet opening angle identical to GRB170817A of $\theta_0 = 5.^\circ2$). In addition to these variables, we assume that the specific internal energy $\eta_0 = 7.9$, boost Lorentz factor $\gamma_B = 9.4$, spectral index $p = 2.15$, electron energy fraction $\epsilon = 0.1$, and magnetic energy fraction $\epsilon_B = 2.5 \times 10^{-4}$ from the updated GRB170817A analysis by Wu & MacFadyen (2019).

We model a range of isotropic kinetic energies (10^{48}–10^{52} erg) and circumburst densities (10^{-6}–1 $\mathrm{cm^{-3}}$), roughly spanning the range of sGRB jet parameters presented by Fong et al. (2015). In addition, we model two jet viewing angles—an on-axis model with $\theta_{obs} = 0^\circ$ and an off-axis model with $\theta_{obs} = 17^\circ$ (see characteristic light curves in Figure 2). In the latter case, the afterglow light curve is still rising after our latest observations of the GW190814 field, and so our limits are primarily sensitive to the luminosity of the afterglow during our last observation epoch, corresponding to Swope and Nickel observations obtained on 2019 September 10–11 with 3σ limiting magnitudes around $r = 20.0$–21.5 mag. Our limits are mostly insensitive to sGRB afterglow light curves with jet viewing angles greater than 17° assuming a jet opening angle of $\theta_0 = 5.^\circ2$ as in Wu & MacFadyen (2018).

4.4. Generic Limits on EM Counterparts

The final set of models we consider is defined empirically using a peak absolute magnitude and linear decline rate in units of $\mathrm{mag\,day^{-1}}$. As kilonovae and sGRBs are rapidly evolving with extremely short rise times (i.e., for kilonovae with physical parameters similar to those of AT 2017gfo and sGRBs viewed on-axis; Drout et al. 2017; Kilpatrick et al. 2017; Arcavi et al. 2017a), we model these generic EM counterparts with a peak brightness at the time of merger as defined by the GW signal. In order to combine our limits across all wavelengths used to follow up GW190814, we further assume that the model counterpart has a flat spectral energy distribution such that the source has the same magnitude in all bands.

Following the procedure outlined above, we combine all of our limits into a likelihood of detection assuming a uniform range of peak absolute magnitudes (from −15 to −20 mag) and decline rates (from 3×10^{-3} to $1\,\mathrm{mag\,day^{-1}}$ in log space) as shown in Figure 8. For comparison, we show our joint limits along with the peak magnitudes and decline rates of various astrophysical transient sources (taken from Siebert et al. 2017).

Although our limiting magnitudes are relatively strong compared with SNe and other luminous transient sources, our

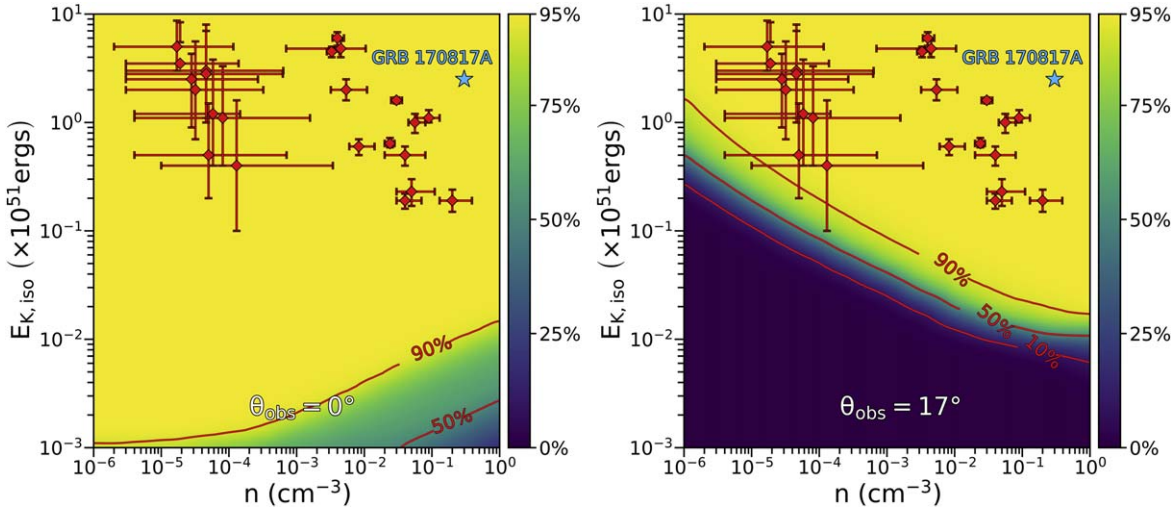

Figure 7. Constraints on the presence of an sGRB viewed on-axis (left, $\theta_{obs} = 0°$) and off-axis (right, $\theta_{obs} = 17°$). In both cases, we show the total observed two-dimensional LVC probability weighted by the likelihood that we would observe a counterpart with a specific explosion energy (E in units of 10^{51} erg s^{-1}) and circumburst density (n in units of cm^{-3}).

empirical limits only extend to −16 mag (∼21 mag at 240 Mpc) for slowly evolving (declining at <0.1 mag day^{-1}) events given that we observed the GW190814 localization over 3–4 days. This places AT 2017gfo−like transients outside of what we can detect, as it began to decline at >0.3 mag day^{-1} blueward of the *i* band at less than 1 day from merger (Drout et al. 2017).

5. Discussion

In this section, we describe the physical implications of our limits in the context of candidate EM counterpart models described in Section 4. As the total area covered by our observations comprises ∼95% of the total two-dimensional probability in the latest GW190814 map, the strongest constraints on EM counterparts are at this significance level. We then discuss further implications of these limits in the context of likely merger models, incorporating the gravitational wave data from Abbott et al. (2020a). Finally, in Section 5.3 we consider the scenario where GW190814 occurred in an AGN disk.

5.1. Joint Limits on Electromagnetic Counterparts

For an AT 2017gfo−like blue kilonova as described in Section 4.1, we estimate a 50% chance of detecting the counterpart at distances <95 Mpc. However, the overall probability of detection given the best-fitting LVC distances for this source is around 1%. As shown in Figure 2, these limits are dominated by our early time observations, as the kilonova models decline rapidly overall. Similarly, the probability of detecting an AT 2017gfo−like red kilonova is extremely low at $\sim 4 \times 10^{-7}$%, which is also mainly constrained by our early time Swope *r*-band and Las Cumbres *i*-band observations. These limits are not constraining for red kilonovae, and we could only detect these models under the assumption that the true distance to GW190814 is much closer (<80 Mpc) than the reported LVC best-fitting distance. Finally, if the counterpart had colors between the blue and red model but the same overall luminosity as AT 2017gfo, the recovery fraction would likely be between the red-only and blue-only numbers.

Inverting these constraints, we are sensitive to the blue kilonova models with $\beta_{ej} = 0.25$ and $M_{ej} > 0.5\,M_\odot$ at 30% significance or $M_{ej} > 0.3\,M_\odot$ at 25% significance. Our strongest constraints for these models come at the edge of our parameter distribution for $M_{ej} = 0.5\,M_\odot$, $v_{ej} = 0.18c$ at 54%. These limits are extreme for GW190814, especially considering that even the most optimistic merger models for a $2.59 \pm 0.08\,M_\odot$ and $23.2^{+1.0}_{-0.9}\,M_\odot$ NSBH merger predict effectively no ejecta mass. However, none of these kilonova limits rule out a detection at high significance, and so we do not consider our limits constraining for kilonovae.

Our limits for GRB models are significantly more constraining given plausible counterparts and small viewing angles. In particular, we find that all on-axis models are ruled out at our maximum 95% likelihood except for the most extreme low-energy (∼10^{48} erg) bursts. In particular, we would have seen the on-axis optical afterglow of a burst similar to any of the bursts described by Fong et al. (2015) or a GRB170817A-like on-axis optical afterglow (following $n = 0.3$ cm^{-3} and $E_k = 2.5 \times 10^{51}$ erg in Murguia-Berthier et al. 2017). Varying the physical parameters of these on-axis, GRB170817-like bursts in Figure 7, we can rule out bursts with a circumburst density $n = 0.3$ cm^{-3} and isotropic equivalent energy $E_k = 2.5 \times 10^{51}$ erg at 95% significance, $n = 0.3$ and $E_k = 2.5 \times 10^{48}$ erg at 50% significance, and $n = 10^{-6}$ cm^{-3} and $E_k = 2.5 \times 10^{51}$ erg at 95% significance. These limits are consistent with the nondetection of GRBs by INTEGRAL, which observed the localization region of GW190814 117° off-axis and constrained the isotropic equivalent energy of the burst to be $<2.1 \times 10^{48}$ erg for a short GRB spectrum with spectral index $\alpha = -0.5$ (assuming $D_L = 239$ Mpc; Molkov et al. 2019). Similar measurements from just a few sources can lead to statistical constraints on jet geometries (Farah et al. 2020).

For larger jet viewing angles (θ_{obs}), but a fixed jet opening angle of $\theta_0 = 5.^\circ 2$, we are increasingly less sensitive to optical afterglows, primarily because the optical luminosity is significantly lower at early times where the majority of our limits are. Beyond $\theta_{obs} > 17°$, we are no longer able to rule out optical afterglows from GRBs similar to those of Fong et al. (2015). In physical terms, we can rule out off-axis optical afterglows from bursts with $n = 0.3$ cm^{-3} and $E_k = 2.5 \times 10^{51}$

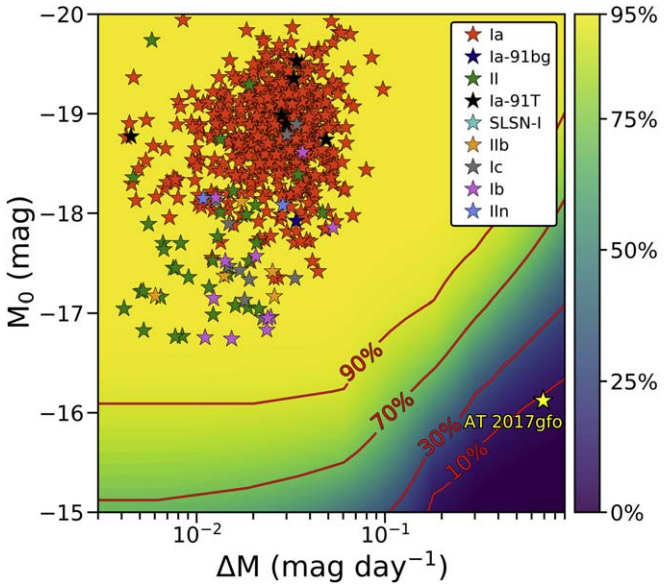

Figure 8. Constraints on the presence of a generic optical counterpart assuming peak magnitude M_0 occurs approximately at the time of merger (t_0) and the source declines at a linear rate ΔM in mag day^{-1}. We further assume that the counterpart has a flat spectral shape at all times such that its magnitude is $M_0 + (t - t_0)\Delta M$ in all bands for all times t. We show the properties of AT 2017gfo with a yellow star with an r-band peak -16.5 mag and decline rate 0.3 mag day^{-1} (based on Drout et al. 2017; Siebert et al. 2017). For comparison, we show the peak magnitudes and decline rates of a range of other optical transients derived from Siebert et al. (2017). We rule out an AT 2017gfo−like counterpart (yellow star) with 6.0% confidence.

erg at 95% significance, $n = 0.3$ and $E_k = 2.5 \times 10^{49}$ erg at 50% significance, and $n = 10^{-6}$ cm^{-3} and $E_k = 2.5 \times 10^{51}$ erg at 62% significance. GW190814 had an inclination angle constrained from its GW signal of 40°–70° (Abbott et al. 2020a), implying that any associated afterglow was likely to be even further off-axis and thus undetectable by our follow-up.

Finally, our limits are comparable to the luminosities of most SNe and optical transients similar to those discussed as interlopers to potential GW counterparts by Siebert et al. (2017). As shown in Figure 8, while we would be able to detect or rule out the presence of virtually all SN subtypes at 241 Mpc, we would likely not be able to detect an AT 2017gfo −like transient (ruled out at 6.0% significance), which is consistent with kilonova model limits.

Assuming a faint counterpart with $\Delta M = 0.68$ mag day^{-1} (similar to the initial r-band decline rate for AT 2017gfo; Drout et al. 2017; Siebert et al. 2017), we rule out sources with $M_{\rm peak} < -17.8$ mag at 50% significance. Similarly, if we assume that the initial magnitude of the source at the time of merger is similar to that of AT 2017gfo with $M_r = -16.1$ mag, we can rule out sources that decline with $\Delta M = 0.06$ mag day^{-1} at 50% significance.

5.2. Combining GW and EM Data for GW190814

With the release of detailed fits to the GW data for GW190814, including component masses, spin constraints, and inclination (Abbott et al. 2020a), we can place more meaningful limits on likely merger scenarios and possible electromagnetic counterparts than with the initial NSBH classification. In particular, the LVC constrained the individual component masses as $2.59 \pm 0.08\,M_\odot$ and $23.2^{+1.0}_{-0.9}$ $M_\odot$ (Abbott et al. 2020a). While these final component masses are consistent with the initial NSBH classification, they imply that there is likely very little ejecta mass under most realistic merger models (Faber et al. 2006; Lee & Ramirez-Ruiz 2007; Ferrari et al. 2010; Roberts et al. 2011; Rosswog et al. 2013), consistent with the `HasRemnant` = 0 statistic.

However, several studies have suggested that the secondary component in this system is likely an NS (Huang et al. 2020; Zevin et al. 2020; Zhang & Li 2020; Tews et al. 2021), although see counterarguments that this component may exceed the maximum NS mass (Akmal et al. 1998; Heger & Woosley 2002; Lattimer & Prakash 2007; Foley et al. 2020). Assuming GW190814 resulted from an NSBH system, our limits place constraints both on parameters that are also constrained by the LVC such as the effective inspiral spin parameter (i.e., the total spin with respect to the orbital plane of the binary, $\chi_{\rm eff}$) and unconstrained parameters such as the NS equation of state. We consider the effect of varying both of these parameters in the context of our limits on kilonova ejecta mass and velocity.

Using our constraints on ejecta mass and velocity from above for a "blue" kilonova, we consider the extent to which we can rule out different values of $\chi_{\rm eff}$. For the former, we consider a range of $\chi_{\rm eff} = 0.01$, 0.5, and 0.995 (where the first value is consistent with the effective-one-body approach waveform parameters, which imply $\chi_{\rm eff} = 0.001^{+0.059}_{-0.056}$, in Abbott et al. 2020a). The last value implies a near maximally spinning BH, which is inconsistent with the general population of BH binaries observed by the LVC (e.g., Abbott et al. 2016b, 2016c, 2017a), but might be obtained in binary populations that evolve from high-mass X-ray binaries (which can have near-maximal spins; McClintock et al. 2006) or evolve through a common-envelope phase (Livio & Soker 1988; Belczynski et al. 2016).

Assuming an ejecta mass and velocity as a function of the binary component masses m_1 and m_2 and fixed $\chi_{\rm eff}$, we predict the total ejecta mass and velocity using equations in Kawaguchi et al. (2016). We then use our blue kilonova models to predict the extent to which we could rule out such a model (Figure 9, where the color corresponds to $P_{\rm model}$ as in Section 4.1). We assume a phenomenological NS equation of state that predicts $R_{\rm NS} = 13.6$ km for a Chandrasekhar-mass NS (H4 in Read et al. 2009), whereas a $2.6\,M_\odot$ NS would have a radius of $\sim$12 km assuming this equation of state and the formalism in Kawaguchi et al. (2016). However, given the extreme mass ratio of GW190814, ejecta masses in the range of our blue kilonova limits would require a near maximally spinning BH and an unrealistic equation of state to produce any ejecta mass.

From the group of models, we only rule out the GW190814 system with significance $P_{\rm model} > 20\%$ (see the definition of $P_{\rm model}$ in Section 4.1) when $\chi_{\rm eff} > 0.995$ (Figure 9). As we decrease the value of $\chi_{\rm eff}$, the value of $P_{\rm model}$ decreases significantly below 0.1%.

Similar analyses were performed by Andreoni et al. (2020)[76], Ackley et al. (2020), and Morgan et al. (2020). Optimistically assuming an equation of state with $\Lambda_{\rm NS} = \lambda c^{10} G^{-4} M_{\rm NS}^{-5} = 800$, where $\lambda = 2/3 k_2 G^{-1} R_{\rm NS}^5$ and k_2 is the Love number, Andreoni et al. (2020) derive effective spin constraints of $\chi < 0.7$. However, we note that their models only assume mass ratios up to merger binary properties with

[76] See their Figure 7.

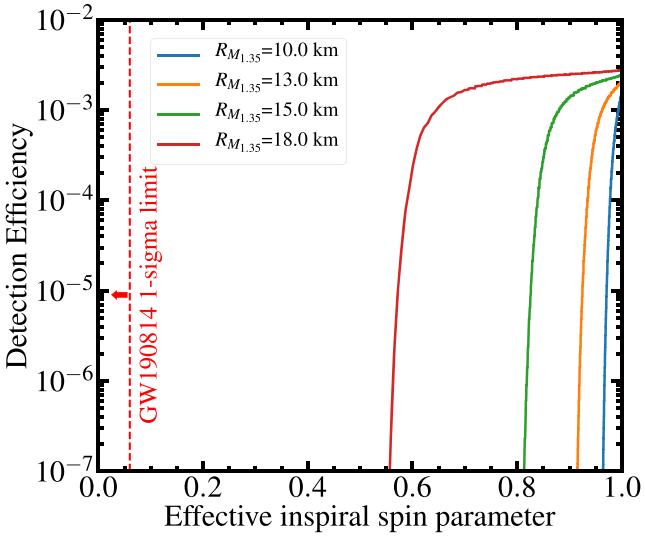

Figure 9. Detection efficiency for kilonovae (described in Section 4.2) as a function of the effective inspiral parameter ($\chi_{\rm eff}$, which is constrained to be <0.06 for GW190814 by Abbott et al. 2020a). We marginalize over the best-fitting component masses for GW190814, which are $23.2^{+0.9}_{-1.0}\,M_\odot$ and $2.59 \pm 0.08\,M_\odot$ based on the effective-one-body approach described by Abbott et al. (2020a). We use these parameters to infer a kilonova ejecta mass and velocity following methods in Kawaguchi et al. (2016) and assuming various equations of state parameterized by radii of a $1.35\,M_\odot$ NS from 10–18 km. Based on these constraints, it is not expected that there would be a significant ejecta mass with parameters inferred for GW190814 even if the secondary is an NS.

$Q = M_2/M_1 = 7$ whereas GW190814 had $Q = 9.0$. Similarly, for a $25\,M_\odot$ BH and DD2 equation of state, Ackley et al. (2020) derive BH spin limits of <0.99 (1σ) for a $1.8\,M_\odot$ NS, although the larger mass of the GW190814 secondary would lead to weaker constraints.

The availability of robust component masses and spin parameters beyond what can be inferred with low-latency LVC parameters (i.e., NSBH classification and `HasRemnant`) has an enormous impact on the predicted observability of EM counterparts. Furthermore, this problem is unique to NSBH follow-up programs where no plausible counterparts have been found. Specific component masses and spins may or may not yield significant ejecta depending on the assumptions we make above about the specific merger model and equation of state.

5.3. Constraints on AGN Counterparts to GW190814

AGNs have been discussed as potential optical counterparts to BBH mergers (Bartos et al. 2017; Antoni et al. 2019; Gröbner et al. 2020), and the discovery of an optical flare timed 34 days after and in the localization region of the BBH merger S190521g/GW190521 (Graham et al. 2020; Abbott et al. 2020b) provides a credible candidate optical counterpart to this phenomenon (although Ashton et al. 2021 suggest there is insufficient evidence to confidently associate the AGN with GW190521). AGN activity is a result of massive gas inflows to a supermassive BH, and as a result of that cause compact object mergers have been explored in the literature (e.g., Stone et al. 2017), and so the compact object merger rate is thought to be significantly enhanced in the disks of these systems. If these systems can form in the disk environment, it is plausible that a significant fraction of LVC counterparts could originate from galaxies with AGNs.

Critically, when a compact object merger occurs in the AGN disk, it can induce an instability in the inflow of gas to the accreting BH, leading to a luminous transient (as is hypothesized to be the case for the S190521g candidate counterpart; McKernan et al. 2012; Antoni et al. 2019; Graham et al. 2020). Thus, the AGN model provides some predictive power for candidate optical counterparts, even in cases where no significant mass of baryonic ejecta is expected from the merger itself.

Here, we examine what constraints can be placed on the distance to and localization of GW190814 under the assumption that the event occurred in a known AGN inside the GW190814 localization region. We analyzed the AGN catalog of Secrest et al. (2015), which is selected from mid-infrared WISE constraints and contains 1.4 million AGNs as faint as $g = 26$ mag. The catalog is estimated to be complete for known AGNs to >84% and for all AGNs with $R < 19$ mag. Therefore, for AGNs with $z < 0.1$, the catalog is expected to be close to >90% complete.

For this analysis, we only consider AGNs that (1) are within the 99th percentile localization region of GW190814, and (2) have a redshift that places it within the 99th percentile volume as described in Section 3. Based on these criteria, we do not identify any AGNs with redshifts listed in the Secrest et al. (2015) catalog or NED.

However, a major caveat to this analysis is that the majority of AGNs do not have measured redshifts, and so most objects would be ruled out for lying outside the volume we consider here. For example, we find 1886 AGNs that match only criterion #1 above. If we consider what fraction of those objects without spectroscopic redshifts lie within 2″ of a source in the PS1-STRM catalog with a photometric redshift that places them in the 99th percentile volume, we are left with only 4 candidates without redshifts in Secrest et al. (2015). We list these sources along with their photometric redshifts in Table 6.

We note that none of these systems is coincident with any of our candidate counterparts to GW190814 (Table 2) or any transients listed in the Transient Name Server to within 5″. Thus, while we consider the AGNs as candidate hosts to GW190814, any hypothetical EM counterparts induced by the merger would have to be low luminosity.

The AGN flare luminosity would scale as the total mass of the merging binary $M^2_{\rm NSBH}$ as in Bartos et al. (2017) and Antoni et al. (2019). Following Equation (5) of Graham et al. (2020) for the total luminosity of such an EM counterpart with radiative efficiency $\eta = 0.1$, kick velocity for the binary in an AGN disk $v_k = 200$ km s^{-1}, disk gas density $\rho = 10^{-10}$ g cm^{-3}, and using the total mass $M_{\rm tot}$ of the GW190814 merger $25.8\,M_\odot$ (Abbott et al. 2020a), we find that the luminosity would be $L = 1.6 \times 10^{44}$ erg s^{-1}, or $M_{\rm bol} = -21.8$ mag, which corresponds to 15.1 mag at $D_L = 241$ Mpc. A source with this brightness is easily ruled out near our maximal efficiency (∼95%) assuming it occurred within the two-week time frame of our observations. That said, the luminosity is easily scaled down for a lower density in the AGN disk, a higher kick velocity, or a lower radiative efficiency in the AGN.

Based on the associated AGN model of Graham et al. (2020), we would expect to see flaring activity of GW190814 if one of these objects had been associated with the merger. Therefore, we examined the ASAS-SN Sky Patrol[77] (Shappee et al. 2014; Kochanek et al. 2017) to determine whether there is any flaring

[77] https://asas-sn.osu.edu/

Table 6
Candidate AGN Hosts for GW190814

Name[a]	α (J2000)	δ (J2000)	Relative Prob.[b]	Redshift[c]
J012323.69-310826.4	01:23:23.70	−31:08:26.43	0.476	0.021 ± 0.002
J005203.80-272348.9	00:52:03.80	−27:23:48.92	0.210	0.079 ± 0.004
J004801.90-215442.2	00:48:01.90	−21:54:42.22	0.082	0.058 ± 0.001
J004002.26-235053.0	00:40:02.27	−23:50:53.03	0.232	0.071 ± 0.004

Notes.
[a] Name of the AGN in the GW190814 localization region in the WISEA catalog from Secrest et al. (2015).
[b] Relative probability of each AGN given the latest GW190814 map provided by Abbott et al. (2020a) such that the sum of all probabilities is unity.
[c] Redshift of matching counterpart given in the PS1-STRM catalog, as all candidate AGNs detected in the GW190814 localization region are matched to sources with photometric redshifts in Beck et al. (2021).

activity potentially associated with the GW event. Although variability is detected for WISEA J005203.80-272348.9, J004801.90-215442.2, and J004002.26-235053.0 after the GW190814 merger, none of them exhibits a $>10^{44}$ erg s^{-1} increase in flux on a timescale of <8 weeks from the GW event. We conclude that these candidates are unlikely to be associated with GW190814.

We also revisit the sources AT 2019nto or AT 2019nup discussed in Section 3.3, which we had previously ruled out as being associated with GW190814 owing to significant premerger variability. This type of variability could occur in the scenario where GW190814 triggered activity in an already active accreting supermassive BH. In both cases, there is a credible optical counterpart, although both are significantly fainter (∼20.8 mag) than we predict for an AGN counterpart at the distance to GW190814. Both events have nearly continuous coverage from the ASAS-SN Sky Patrol up to ∼170 days from the time of merger. A source is detected at the site of AT 2019nto twice during that interval >100 days from the time of merger, and AT 2019nup is detected almost continuously during that time but with no >1 mag increases in brightness. If either of these objects is associated with an AGN from GW190814, that event would need to occur with an extremely low radiative efficiency ($\eta < 0.01$) or from a disk with a much lower gas density ($\rho < 10^{-12}$ g cm^{-3}) compared with the model presented above.

One of the primary difficulties in detecting an AGN counterpart to a GW source is the dynamical timescale for perturbations in the disk to induce enhanced accretion in the AGN and trigger a flare. This dynamical timescale $t_{\rm dyn}$ (Equation (6) of Graham et al. 2020) is only ∼5 days assuming that the kick velocity $v_k = 200$ km s^{-1}. However, $t_{\rm dyn}$ scales as v_k^{-3}, and so for a marginally lower kick velocity it could easily be outside of the window of our observations (and the flare of significantly lower luminosity, as above). While this velocity needs to remain small enough that the system remains bound to the disk of the AGN to trigger a flare, scaling the kick velocity in a fixed-mass AGN and at a fixed orbital semimajor axis suggests that $v_k \propto M_{\rm tot}^{-1/2}$, or ∼400 km s^{-1} compared with 200 km s^{-1} for the BBH system of Graham et al. (2020).

Regardless of the presence of an EM counterpart to validate the AGN counterpart hypothesis, if we assume that the event occurred in such an environment we can obtain separate constraints on the distance to this event. There is a single AGN (WISEA J004506.98-250147.0) that represents >50% of the normalized two-dimensional probability for GW190814 after renormalizing under the assumption that one of these candidates is the host. Accounting for the individual uncertainties and weighting by this local two-dimensional probability, we find that the best-fitting redshift is $z = 0.052 \pm 0.017$ or $D_L = 233 \pm 80$ Mpc. Compared with the GW190814 distance marginalized over the entire localization region, this inferred distance is more uncertain.

6. Conclusions

We have presented results from the joint follow-up observations of the LVC NSBH merger GW190814. Our combined constraints from optical imaging and spectroscopy demonstrate the following.

1. There are no plausible optical counterparts detected by our programs or those of any other optical or radio follow-up groups (Dobie et al. 2019a; Gomez et al. 2019b; Ackley et al. 2020; Andreoni et al. 2020; Morgan et al. 2020; Thakur et al. 2020; Vieira et al. 2020; Watson et al. 2020; Alexander et al. 2021; de Wet et al. 2021). Given criteria that we describe in Section 3, we are able to rule out all known transient sources detected within the 99th percentile localization of GW190814 and discovered within two weeks of the merger time given by the LVC.
2. Given that there are no plausible counterparts, we are able to rule out kilonovae, GRBs, and SN-like optical counterparts to deep limits using the joint limits from all follow-up observations performed in this study. While our limits are not constraining in the context of red (low Y_e) kilonovae, we rule out blue kilonovae ($Y_e > 0.4$) with $v_{\rm ej} = 0.25c$ and $M_{\rm ej} > 0.3\,M_\odot$ to 25% significance. We also rule out sGRBs similar to those of Fong et al. (2015) at ∼95% significance for on-axis events and at >50% significance for viewing angles $\theta_{\rm obs} < 17°$. Finally, while our limits can probe luminosities as deep as −16 mag (21 mag at 240 Mpc) across most of the localization region, we cannot rule out events this faint with decline rates comparable to AT 2017gfo at >0.3 mag day^{-1}.
3. Using our joint limits on optical counterparts, we combine our EM follow-up data with the GW data of Abbott et al. (2020a) to consider scenarios in which NSBH systems would be detectable. We find that only for near maximally spinning BHs (where the NSBH system has $\chi_{\rm eff} > 0.995$) can we rule out merger scenarios similar

to GW190814 with appreciable (>20%) significance. While these parameters are inconsistent with those observed from GW190814 (with $\chi_{\rm eff} < 0.06$ for all waveform models), these limits provide a baseline for plausible constraints on future NSBH counterparts.

4. We consider the possibility that GW190814 occurred in the disk of an AGN similar to the potential counterpart to the BBH merger S190521g proposed by Graham et al. (2020). Analyzing AGN catalogs, we find only seven galaxies with AGNs and localized within the volume of GW190814. This is more than three orders of magnitude smaller than the total number of galaxies in the localization region and may provide an efficient search strategy for targeting electromagnetic emission for future compact object mergers.

This analysis was conducted on data collected by three GW follow-up efforts: 1M2H, KAIT, and Las Cumbres, each with independent observational strategies. Each collaboration used a different set of filters, targeting selection, and timescales that offer a unique constraints on EM counterparts to GW190814. Our combined data sets enable a more comprehensive and uniform analysis than was immediately possible after the discovery of the event. The future of GW follow-up efforts will benefit from similar analyses using data sharing and communication media such as the Treasure Map (Wyatt et al. 2020) and the Gamma-ray Coordinates Network (Barthelmy et al. 1995), open-source software and analysis tools such as `teglon` and `gwemlightcurves` (Coughlin et al. 2020b), and increased collaboration within the GW/EM community.

We thank T. M. Davis, W. Fong, and J. X. Prochaska for helpful comments on this manuscript, as well as J. J. Hermes and S. Points for support with the SOAR observations. We appreciate the expert assistance of the staffs at the various observatories where data were obtained.

Much of this work was performed during the "Astrophysics in the LIGO/Virgo Era" meeting at the Aspen Center for Physics during Summer 2019, with C.D.K., D.A.C., I.A., D.O. J., C.R.-B., E.R.-R., A.R., and M.R.S. all participating. The Aspen Center for Physics is supported by National Science Foundation (NSF) grant PHY-1607611.

The UCSC team is supported in part by NASA grant NNG17PX03C, NSF grant AST-1815935, the Gordon & Betty Moore Foundation, the Heising-Simons Foundation, and by fellowships from the David and Lucile Packard Foundation to R.J.F. D.A.C. acknowledges support from the NSF Graduate Research Fellowship under grant DGE1339067. A.V.F.'s group at UC Berkeley is grateful for financial assistance from the Miller Institute for Basic Research in Science (in which A.V.F. is a Miller Senior Fellow), the Christopher R. Redlich Fund, Sunil Nagaraj, Landon Noll (K.C.P. is a Nagaraj-Noll Graduate Fellow), Steven Nelson (S.S.V. is a Steven Nelson Graduate Fellow), and many other individual donors. D.E.H. was supported by NSF grants PHY-1708081 and PHY-2011997, and the Kavli Institute for Cosmological Physics at the University of Chicago through an endowment from the Kavli Foundation. Time-domain research by D.J.S. is supported by NSF grants AST-1821987, 1813466, and 1908972, and by the Heising-Simons Foundation under grant #2020-1864. F.O.E. acknowledges support from FONDECYT grant 1201223. I. A. is a CIFAR Azrieli Global Scholar in the Gravity and the Extreme Universe Program and acknowledges support from that program, from the European Research Council (ERC) under the European Union's Horizon 2020 research and innovation program (grant agreement 852097), from the Israel Science Foundation (grant 2752/19), from the United States—Israel Binational Science Foundation (BSF), and from the Israeli Council for Higher Education Alon Fellowship. J.B. is supported by NSF grants AST-1313484 and AST-1911225, as well as by NASA grant 80NSSC19kf1639. J.C. acknowledges support from the Australian Research Council Centre of Excellence for Gravitational Wave Discovery (OzGrav) project CE170100004. J.G.B. is supported by MINECO project PGC2018-094773-B-C32. L.S. S. acknowledges the financial support from FAPESP through grant #2020/03301-5. M.M. is supported by CONICET, CNPq, and FAPERJ. M.R.S. is supported by the NSF Graduate Research Fellowship Program under grant 184240. The U.M. team is supported by NSF grant AST-1910719 and fellowships from the Alfred P. Sloan Foundation and the Cottrell Scholar Award to M.S.-S. N.H. acknowledges support for this work by Israel Science Foundation grant 541/17. R.R.d.C. acknowledges financial support from FAPESP through grant #2014/11156-4. R.R.M. acknowledges partial support from project BASAL AFB-170002 as well as FONDECYT project 1170364. S.B.R. acknowledges support from Conselho Nacional de Desenvolvimento Científico e Tecnológico—CNPq. T.D. is supported by ARC grant FL180100168. T.L.P. acknowledges financial support from CAPES.

This work includes data obtained with the Swope Telescope at Las Campanas Observatory, Chile, as part of the Swope Time Domain Key Project (PI Piro; Co-Is Burns, Cowperthwaite, Dimitriadis, Drout, Foley, French, Holoien, Hsiao, Kilpatrick, Madore, Phillips, and Rojas-Bravo). This work makes use of observations from the LCO Network. The LCO Group is supported by NSF grant AST-1911151.

Some of the data presented herein were obtained at the W. M. Keck Observatory, which is operated as a scientific partnership among the California Institute of Technology, the University of California, and NASA. The Observatory was made possible by the generous financial support of the W. M. Keck Foundation. The authors wish to recognize and acknowledge the very significant cultural role and reverence that the summit of Maunakea has always had within the indigenous Hawaiian community. We are most fortunate to have the opportunity to conduct observations from this mountain.

Based in part on observations obtained at the Southern Astrophysical Research (SOAR) telescope, which is a joint project of the Ministério da Ciência, Tecnologia, Inovações e Comunicações (MCTIC) do Brasil, the U.S. National Optical Astronomy Observatory (NOAO), the University of North Carolina at Chapel Hill (UNC), and Michigan State University (MSU).

Research at Lick Observatory is partially supported by a generous gift from Google. KAIT and its ongoing operation were made possible by donations from Sun Microsystems, Inc., the Hewlett-Packard Company, AutoScope Corporation, Lick Observatory, the NSF, the University of California, the Sylvia and Jim Katzman Foundation, and the TABASGO Foundation.

Software: `astropy` (Astropy Collaboration et al. 2013), `DoPhot` (Schechter et al. 1993), `hotpants` (Becker 2015),

`healpy` (Zonca et al. 2019), `IDL` (Landsman 1993), `LCOGTSNpipe` (Valenti et al. 2016), `ligo.skymap` (Singer et al. 2016a, 2016b), `PypeIt` (Prochaska et al. 2020a, 2020b), `SExtractor` (Bertin & Arnouts 1996), `teglon`.

Facilities: Las Cumbres (SINISTRO), Lick/Shane 3 m (Kast), KAIT, Keck:I (MOSFIRE), Keck:II (DEIMOS), Nickel (Direct 2K), SOAR (Goodman), Swope (Direct 4K), Thacher (ACP).

Appendix
Analysis of Candidate Distribution around GW190814

As a test to evaluate whether our candidate distribution is biased compared with our search, we analyzed the distribution of candidates around GW190814. Figure 10 shows the number of candidates per 0.21 deg^2 cell around GW190814. We note that the southern node in the GW190814 90% localization map has significantly fewer candidates than the upper node, which reflects the fact that our search was significantly shallower in this region.

In the northern node, there are 114 cells within the 99% localization of GW190814 and 152 candidates, or roughly 6.2 candidates deg^{-2}. Regions of significantly fewer candidates near the center of GW190814 therefore appear to be $\sim 1\sigma$ outliers in the overall distribution of candidates. However, there are a handful of regions with significantly more candidates; at most nine candidates occur within a single cell of the map. These candidates appear clustered and appear to overlap with imaging from Swope, Las Cumbres, and Thacher, with the deepest depths in our search. We infer that the increased incidence of candidates in this region is also a product of enhanced search depth. However, a comparison between the incidence of candidates and stellar mass, for example by comparing to the cumulative luminosity of galaxies in these cells from the `GLADE` catalog (Dálya et al. 2018), might also reveal a correlation.

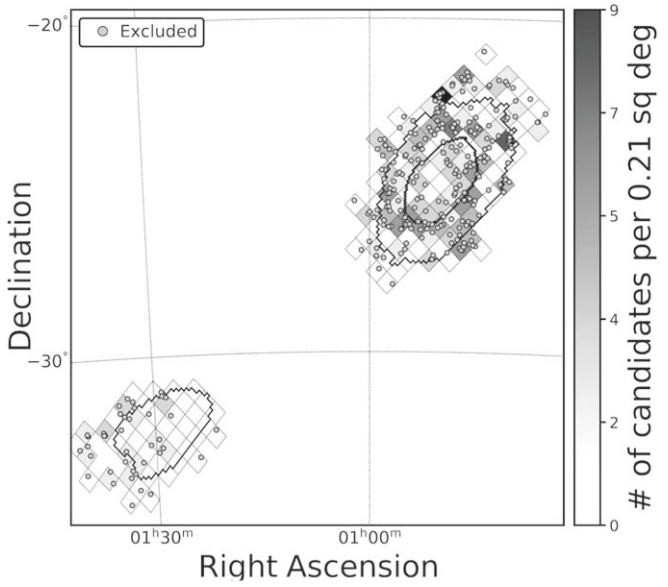

Figure 10. The distribution of candidates on the sky compared with the GW190814 localization region of Abbott et al. (2020a). We segment the map into 0.21 deg^2 cells, with each cell ranging from 0 to 9 candidates per cell. Each individual candidate is indicated as a gray circle.

ORCID iDs

Charles D. Kilpatrick https://orcid.org/0000-0002-5740-7747
David A. Coulter https://orcid.org/0000-0003-4263-2228
Iair Arcavi https://orcid.org/0000-0001-7090-4898
Thomas G. Brink https://orcid.org/0000-0001-5955-2502
Georgios Dimitriadis https://orcid.org/0000-0001-9494-179X
Alexei V. Filippenko https://orcid.org/0000-0003-3460-0103
Ryan J. Foley https://orcid.org/0000-0002-2445-5275
David O. Jones https://orcid.org/0000-0002-6230-0151
Daniel Kasen https://orcid.org/0000-0002-5981-1022
Martin Makler https://orcid.org/0000-0003-2206-2651
Anthony L. Piro https://orcid.org/0000-0001-6806-0673
César Rojas-Bravo https://orcid.org/0000-0002-7559-315X
David J. Sand https://orcid.org/0000-0003-4102-380X
Jonathan J. Swift https://orcid.org/0000-0002-9486-818X
Douglas Tucker https://orcid.org/0000-0001-7211-5729
WeiKang Zheng https://orcid.org/0000-0002-2636-6508
James T. Annis https://orcid.org/0000-0002-0609-3987
Tristan G. Bachmann https://orcid.org/0000-0002-6119-5353
Joshua S. Bloom https://orcid.org/0000-0002-7777-216X
Clecio R. Bom https://orcid.org/0000-0003-4383-2969
K. Azalee Bostroem https://orcid.org/0000-0002-4924-444X
Dillon Brout https://orcid.org/0000-0001-5201-8374
Jamison Burke https://orcid.org/0000-0003-0035-6659
Robert E. Butler https://orcid.org/0000-0003-2789-3817
Abdo Campillay https://orcid.org/0000-0002-3829-9920
Christopher J. Conselice https://orcid.org/0000-0003-1949-7638
Jeff Cooke https://orcid.org/0000-0001-5703-2108
Kristen C. Dage https://orcid.org/0000-0002-8532-4025
Reinaldo R. de Carvalho https://orcid.org/0000-0002-1283-3363
Thomas de Jaeger https://orcid.org/0000-0001-6069-1139
Shantanu Desai https://orcid.org/0000-0002-0466-3288
Alyssa Garcia https://orcid.org/0000-0001-9578-6322
Juan Garcia-Bellido https://orcid.org/0000-0002-9370-8360
Mandeep S. S. Gill https://orcid.org/0000-0003-2524-5154
Na'ama Hallakoun https://orcid.org/0000-0002-0430-7793
Kenneth Herner https://orcid.org/0000-0001-6718-2978
Daichi Hiramatsu https://orcid.org/0000-0002-1125-9187
Daniel E. Holz https://orcid.org/0000-0002-0175-5064
Adam M. Kawash https://orcid.org/0000-0003-0071-1622
Curtis McCully https://orcid.org/0000-0001-5807-7893
Brian D. Metzger https://orcid.org/0000-0002-4670-7509
Robert Morgan https://orcid.org/0000-0002-7016-5471
Yukei S. Murakami https://orcid.org/0000-0002-8342-3804
Felipe Olivares E. https://orcid.org/0000-0002-5115-6377
Antonella Palmese https://orcid.org/0000-0002-6011-0530
Kishore C. Patra https://orcid.org/0000-0002-1092-6806
Maria E. S. Pereira https://orcid.org/0000-0002-7131-7684
Thallis L. Pessi https://orcid.org/0000-0001-6540-0767
Enrico Ramirez-Ruiz https://orcid.org/0000-0003-2558-3102
Sandro Barboza Rembold https://orcid.org/0000-0003-0880-5738
Armin Rest https://orcid.org/0000-0002-4410-5387
Ósmar Rodríguez https://orcid.org/0000-0001-8651-8772
Luidhy Santana-Silva https://orcid.org/0000-0003-3402-6164
Matthew R. Siebert https://orcid.org/0000-0003-2445-3891
J. Allyn Smith https://orcid.org/0000-0002-6261-4601
Marcelle Soares-Santos https://orcid.org/0000-0001-6082-8529
Benjamin E. Stahl https://orcid.org/0000-0002-3169-3167
Jay Strader https://orcid.org/0000-0002-1468-9668
Samaporn Tinyanont https://orcid.org/0000-0002-1481-4676
Brad E. Tucker https://orcid.org/0000-0002-4283-5159
Stefano Valenti https://orcid.org/0000-0001-8818-0795

Sergiy S. Vasylyev https://orcid.org/0000-0002-4951-8762
Matthew P. Wiesner https://orcid.org/0000-0001-8653-7738
Keto D. Zhang https://orcid.org/0000-0002-9955-8797

References

Abadie, J., Abbott, B. P., Abbott, R., et al. 2011, PhRvL, 107, 271102
Abbott, B. P., Abbott, R., Abbott, T. D., et al. 2016a, PhRvL, 116, 061102
Abbott, B. P., Abbott, R., Abbott, T. D., et al. 2016b, PhRvX, 6, 041015
Abbott, B. P., Abbott, R., Abbott, T. D., et al. 2016c, PhRvL, 116, 241102
Abbott, B. P., Abbott, R., Abbott, T. D., et al. 2016d, PhRvL, 116, 241103
Abbott, B. P., Abbott, R., Abbott, T. D., et al. 2017a, PhRvL, 119, 141101
Abbott, B. P., Abbott, R., Abbott, T. D., et al. 2017b, PhRvL, 118, 221101
Abbott, B. P., Abbott, R., Abbott, T. D., et al. 2017c, ApJL, 848, L13
Abbott, B. P., Abbott, R., Abbott, T. D., et al. 2018a, PhRvL, 121, 161101
Abbott, B. P., Abbott, R., Abbott, T. D., et al. 2021b, ApJ, 909, 218
Abbott, B. P., Abbott, R., Adhikari, R., et al. 2009, RPPh, 72, 076901
Abbott, R., Abbott, T. D., Abraham, S., et al. 2020a, ApJL, 896, L44
Abbott, R., Abbott, T. D., Abraham, S., et al. 2020b, PhRvL, 125, 101102
Abbott, R., Abbott, T. D., Abraham, S., et al. 2021a, PhRvX, 11, 021053
Abbott, T. M. C., Abdalla, F. B., Allam, S., et al. 2018b, ApJS, 239, 18
Ackley, K., Amati, L., Barbieri, C., et al. 2020, A&A, 643, A113
Aggarwal, K., Budavári, T., Deller, A. T., et al. 2021, ApJ, 911, 95
Akmal, A., Pandharipande, V. R., & Ravenhall, D. G. 1998, PhRvC, 58, 1804
Al, M. S. E. 2019a, Transient Name Server Discovery Report, 2019-1509
Al, M. S. E. 2019b, Transient Name Server Discovery Report, 2019-1536
Al, M. S. E. 2019c, Transient Name Server Discovery Report, 2019-1563
Al, M. S. E. 2019d, Transient Name Server Discovery Report, 2019-1604
Al, M. S. E. 2019e, Transient Name Server Discovery Report, 2019-1615
Alard, C., & Lupton, R. H. 1998, ApJ, 503, 325
Alexander, K. D., Schroeder, G., Paterson, K., et al. 2021, ApJ, 923, 66
Anand, N., Shahid, M., & Resmi, L. 2018, MNRAS, 481, 4332
Andreoni, I., & Goldstein, D. 2019a, Transient Name Server Discovery Report, 2019-1496
Andreoni, I., & Goldstein, D. 2019b, Transient Name Server Discovery Report, 2019-1507
Andreoni, I., & Goldstein, D. 2019c, Transient Name Server Discovery Report, 2019-1516
Andreoni, I., & Goldstein, D. 2019d, Transient Name Server Discovery Report, 2019-1525
Andreoni, I., & Goldstein, D. 2019e, Transient Name Server Discovery Report, 2019-1562
Andreoni, I., Goldstein, D. A., Ahumada, T., et al. 2019b, GCN, 25362, 1
Andreoni, I., Goldstein, D. A., Anand, S., et al. 2019a, ApJL, 881, L16
Andreoni, I., Goldstein, D. A., Kasliwal, M. M., et al. 2020, ApJ, 890, 131
Antier, S., Agayeva, S., Aivazyan, V., et al. 2020, MNRAS, 492, 3904
Antoni, A., MacLeod, M., & Ramirez-Ruiz, E. 2019, ApJ, 884, 22
Arcavi, I., Hosseinzadeh, G., Howell, D. A., et al. 2017a, Natur, 551, 64
Arcavi, I., McCully, C., Hosseinzadeh, G., et al. 2017b, ApJL, 848, L33
Ashton, G., Ackley, K., Magaña Hernandez, I., & Piotrzkowski, B. 2021, CQGra, 38, 235004
Astropy Collaboration, Robitaille, T. P., Tollerud, E. J., et al. 2013, A&A, 558, A33
Barro, G., Trump, J. R., Koo, D. C., et al. 2014, ApJ, 795, 145
Barthelmy, S. D., Butterworth, P., Cline, T. L., et al. 1995, Ap&SS, 231, 235
Bartos, I., Kocsis, B., Haiman, Z., & Márka, S. 2017, ApJ, 835, 165
Bauer, F. E., Fruchter, A. S., Gonzalez Lopez, J., et al. 2019, GCN, 25801, 1
Beck, R., Szapudi, I., Flewelling, H., et al. 2021, MNRAS, 500, 1633
Becker, A. 2015, HOTPANTS: High Order Transform of PSF ANd Template Subtraction, Astrophysics Source Code Library, ascl:1504.004
Behroozi, P. S., Ramirez-Ruiz, E., & Fryer, C. L. 2014, ApJ, 792, 123
Belczynski, K., Holz, D. E., Bulik, T., & O'Shaughnessy, R. 2016, Natur, 534, 512
Bell, E. F., McIntosh, D. H., Katz, N., & Weinberg, M. D. 2003, ApJS, 149, 289
Bertin, E., & Arnouts, S. 1996, A&AS, 117, 393
Bilicki, M., Jarrett, T. H., Peacock, J. A., Cluver, M. E., & Steward, L. 2014, ApJS, 210, 9
Blondin, S., & Tonry, J. L. 2007, ApJ, 666, 1024
Brown, J. S., Foley, R. J., Coulter, D. A., et al. 2019, GCN, 25344, 1
Brown, T. M., Baliber, N., Bianco, F. B., et al. 2013, PASP, 125, 1031
Buckley, D., Ciroi, S., Gromadzki, M., et al. 2019, Transient Name Server Classification Report, 2019-1652
Cartier, R., Briceño, C., Olivares, F., et al. 2019, GCN, 25784, 1
Castro-Tirado, A. J., Valeev, A. F., Hu, Y. D., et al. 2019, GCN, 25543, 1
Chambers, K. C., Boer, T. D., Bulger, J., et al. 2019, Transient Name Server Discovery Report, 2019-1584
Chung, S. M., Eisenhardt, P. R., Gonzalez, A. H., et al. 2011, ApJ, 743, 34
Coughlin, M. W., Ahumada, T., Anand, S., et al. 2019, ApJL, 885, L19
Coughlin, M. W., Antier, S., Dietrich, T., et al. 2020b, NatCo, 11, 4129
Coughlin, M. W., Dietrich, T., Antier, S., et al. 2020a, MNRAS, 492, 863
Coulter, D. A., Foley, R. J., Kilpatrick, C. D., et al. 2017, Sci, 358, 1556
Cowperthwaite, P. S., Berger, E., Villar, V. A., et al. 2017, ApJL, 848, L17
Cutri, R. M., Skrutskie, M. F., van Dyk, S., et al. 2003, IRSA 2MASS All-SkyPoint Source Catalog, NASA/IPAC Infrared Science Archive, http://irsa.ipac.caltech.edu/applications/Gator/
Dálya, G., Galgóczi, G., Dobos, L., et al. 2018, MNRAS, 479, 2374
de Wet, S., Groot, P. J., Bloemen, S., et al. 2021, A&A, 649, A72
Dimitriadis, G., Brown, J. S., Seibert, M. R., et al. 2019, GCN, 25395, 1
Dobie, D., Stewart, A., Murphy, T., et al. 2019a, ApJL, 887, L13
Dobie, D., Stewart, A., Wang, Z., et al. 2019b, GCN, 25445, 1
Drout, M. R., Piro, A. L., Shappee, B. J., et al. 2017, Sci, 358, 1570
Drout, M. R., Simon, J. D., Shappe, B. J., et al. 2017, GCN, 21547, 1
Duffell, P. C., & MacFadyen, A. I. 2013, ApJL, 776, L9
Faber, J. A., Baumgarte, T. W., Shapiro, S. L., & Taniguchi, K. 2006, ApJL, 641, L93
Faber, S. M., Phillips, A. C., Kibrick, R. I., et al. 2003, Proc. SPIE, 4841, 1657
Farah, A., Essick, R., Doctor, Z., Fishbach, M., & Holz, D. E. 2020, ApJ, 895, 108
Fattoyev, F. J., Horowitz, C. J., Piekarewicz, J., & Reed, B. 2020, PhRvC, 102, 065805
Ferrari, V., Gualtieri, L., & Pannarale, F. 2010, PhRvD, 81, 064026
Filippenko, A. V., Li, W. D., Treffers, R. R., & Modjaz, M. 2001, in ASP Conf. Ser. 246, IAU Coll. 183: Small Telescope Astronomy on Global Scales, ed. B. Paczynski, W.-P. Chen, & C. Lemme (San Francisco, CA: ASP), 121
Flewelling, H. A., Magnier, E. A., Chambers, K. C., et al. 2020, ApJS, 251, 7
Foley, R. J., Coulter, D. A., Kilpatrick, C. D., et al. 2020, MNRAS, 494, 190
Fong, W., & Berger, E. 2013, ApJ, 776, 18
Fong, W., Berger, E., Blanchard, P. K., et al. 2017, ApJL, 848, L23
Fong, W., Berger, E., Margutti, R., & Zauderer, B. A. 2015, ApJ, 815, 102
Gaia Collaboration, Brown, A. G. A., Vallenari, A., et al. 2018, A&A, 616, A1
Ganeshalingam, M., Li, W., Filippenko, A. V., et al. 2010, ApJS, 190, 418
Godzieba, D. A., Radice, D., & Bernuzzi, S. 2021, ApJ, 908, 122
Goldstein, D., Anand, S. & Growth Collaboration 2019a, GCN, 25394, 1
Goldstein, D., Andreoni, I., Hankins, M., et al. 2019b, GCN, 25393, 1
Goldstein, D. A., Andreoni, I., Nugent, P. E., et al. 2019c, ApJL, 881, L7
Gomez, S., Hosseinzadeh, G., Blanchard, P., et al. 2019a, Transient Name Server Classification Report, 2019-1643
Gomez, S., Hosseinzadeh, G., Cowperthwaite, P. S., et al. 2019b, ApJL, 884, L55
Górski, K. M., Hivon, E., Banday, A. J., et al. 2005, ApJ, 622, 759
Graham, M. J., Ford, K. E. S., McKernan, B., et al. 2020, PhRvL, 124, 251102
Gröbner, M., Ishibashi, W., Tiwari, S., Haney, M., & Jetzer, P. 2020, A&A, 638, A119
Guevel, D., & Hosseinzadeh, G. 2017, Dguevel/Pyzogy: Initial Release, v0.0.1, Zenodo, doi:10.5281/zenodo.1043973
Heger, A., & Woosley, S. E. 2002, ApJ, 567, 532
Henden, A. A., Levine, S., Terrell, D., & Welch, D. L. 2015, AAS Meeting, 225, 336.16
Herner, K. 2019a, Transient Name Server Discovery Report, 2019-1508
Herner, K. 2019b, Transient Name Server Discovery Report, 2019-1579
Herner, K., Palmese, A., Soares-Santos, M., et al. 2019a, GCN, 25373, 1
Herner, K., Palmese, A., Soares-Santos, M., et al. 2019b, GCN, 25398, 1
Herner, K., & Team, B. O. T. D. 2019, Transient Name Server Discovery Report, 2019-1526
Hiramatsu, D., Arcavi, I., Howell, D. A., et al. 2019a, Transient Name Server Classification Report, 2019-1522
Hiramatsu, D., Howell, D. A., Arcavi, I., et al. 2019b, GCN, 25422, 1
Hosseinzadeh, G., Cowperthwaite, P. S., Gomez, S., et al. 2019, ApJL, 880, L4
Huang, K., Hu, J., Zhang, Y., & Shen, H. 2020, ApJ, 904, 39
Huber, M., Smith, K. W., Chambers, K., et al. 2019, GCN, 25356, 1
Jaodand, A., Campana, S., Brightman, M., et al. 2019, GCN, 25822, 1
Japelj, J., Kankare, E., Kool, E., et al. 2019, GCN, 25526, 1
Jayasinghe, T., Stanek, K. Z., Kochanek, C. S., et al. 2019, MNRAS, 485, 961
Jester, S., Schneider, D. P., Richards, G. T., et al. 2005, AJ, 130, 873
Johnston, S., Bailes, M., Bartel, N., et al. 2007, PASA, 24, 174
Johnston, S., Taylor, R., Bailes, M., et al. 2008, ExA, 22, 151
Jones, D. H., Read, M. A., Saunders, W., et al. 2009, MNRAS, 399, 683
Joss, P. C., & Rappaport, S. A. 1984, ARA&A, 22, 537

Kanakis-Pegios, A., Koliogiannis, P. S., & Moustakidis, C. C. 2021, Symmetry, 13, 183
Kasen, D., Fernández, R., & Metzger, B. D. 2015, MNRAS, 450, 1777
Kasen, D., Metzger, B., Barnes, J., Quataert, E., & Ramirez-Ruiz, E. 2017, Natur, 551, 80
Kasliwal, M. M., Nakar, E., Singer, L. P., et al. 2017, Sci, 358, 1559
Kawaguchi, K., Kyutoku, K., Shibata, M., & Tanaka, M. 2016, ApJ, 825, 52
Kilpatrick, C. D., Coulter, D. A., Brown, J. S., et al. 2019, GCN, 25350, 1
Kilpatrick, C. D., Foley, R. J., Drout, M. R., et al. 2018, MNRAS, 473, 4805
Kilpatrick, C. D., Foley, R. J., Kasen, D., et al. 2017, Sci, 358, 1583
Kocevski, D. & Fermi-GBM Team 2019, GCN, 25326, 1
Kochanek, C. S., Shappee, B. J., Stanek, K. Z., et al. 2017, PASP, 129, 104502
Kurtz, M. J., & Mink, D. J. 1998, PASP, 110, 934
Landolt, A. U. 1992, AJ, 104, 340
Landsman, W. B. 1993, in ASP Conf. Ser. 52, Astronomical Data Analysis Software and Systems II, ed. R. J. Hanisch, R. J. V. Brissenden, & J. Barnes (San Francisco, CA: ASP), 246
Lattimer, J. M., & Prakash, M. 2007, PhR, 442, 109
Lazarus, P., Freire, P. C. C., Allen, B., et al. 2016, ApJ, 831, 150
Lazzati, D., Deich, A., Morsony, B. J., & Workman, J. C. 2017, MNRAS, 471, 1652
Lee, W. H., & Ramirez-Ruiz, E. 2007, NJPh, 9, 17
Li, L.-X., & Paczyński, B. 1998, ApJL, 507, L59
Li, W., Filippenko, A. V., Chornock, R., & Jha, S. 2003, PASP, 115, 844
LIGO Scientific Collaboration, Aasi, J., Abbott, B. P., et al. 2015, CQGra, 32, 074001
LIGO Scientific Collaboration & Virgo Collaboration 2019a, GCN, 25324, 1
LIGO Scientific Collaboration & Virgo Collaboration 2019b, GCN, 25333, 1
Lippuner, J., & Roberts, L. F. 2015, ApJ, 815, 82
Livio, M., & Soker, N. 1988, ApJ, 329, 764
Lopez-Cruz, O., Castro-Tirado, A. J., Macri, L., et al. 2019, GCN, 25419, 1
Lundquist, M. J., Paterson, K., Fong, W., et al. 2019, ApJL, 881, L26
McClintock, J. E., Shafee, R., Narayan, R., et al. 2006, ApJ, 652, 518
McConnell, D., Allison, J. R., Bannister, K., et al. 2016, PASA, 33, e042
McCully, C., Volgenau, N. H., Harbeck, D.-R., et al. 2018, Proc. SPIE, 10707, 107070K
McKernan, B., Ford, K. E. S., Lyra, W., & Perets, H. B. 2012, MNRAS, 425, 460
McLean, I. S., Steidel, C. C., Epps, H. W., et al. 2012, Proc. SPIE, 8446, 84460J
Metzger, B. D. 2017, LRR, 20, 3
Metzger, B. D. 2019, LRR, 23, 1
Metzger, B. D., & Fernández, R. 2014, MNRAS, 441, 3444
Metzger, B. D., Martínez-Pinedo, G., Darbha, S., et al. 2010, MNRAS, 406, 2650
Rodríguez, Ó., Meza-Retamal, N., Quirola, J., et al. 2019, GCN, 25423, 1
Miller, J., & Stone, R. 1993, Lick Obs. Tech. Rep. 66
Molkov, S., Mereghetti, S., Savchenko, V., et al. 2019, GCN, 25323, 1
Mooley, K. P., Nakar, E., Hotokezaka, K., et al. 2018, Natur, 554, 207
Morgan, R., Soares-Santos, M., Annis, J., et al. 2020, ApJ, 901, 83
Murguia-Berthier, A., Ramirez-Ruiz, E., De Colle, F., et al. 2021, ApJ, 908, 152
Murguia-Berthier, A., Ramirez-Ruiz, E., Kilpatrick, C. D., et al. 2017, ApJL, 848, L34
Oke, J. B., & Gunn, J. E. 1983, ApJ, 266, 713
Palmer, D. M., Barthelmy, S. D., Lien, A. Y., et al. 2019, GCN, 25341, 1
Palmese, A., deVicente, J., Pereira, M. E. S., et al. 2020, ApJL, 900, L33
Paterson, K., Lundquist, M. J., Rastinejad, J. C., et al. 2021, ApJ, 912, 128
Planck Collaboration, Ade, P. A. R., Aghanim, N., et al. 2016 A&A, 594, A13
Pozanenko, A. S., Minaev, P. Y., Grebenev, S. A., & Chelovekov, I. V. 2020, AstL, 45, 710
Press, W. H., & Thorne, K. S. 1972, ARA&A, 10, 335
Prochaska, J., Hennawi, J., Westfall, K., et al. 2020a, JOSS, 5, 2308
Prochaska, J. X., Hennawi, J., Cooke, R., et al. 2020b, pypeit/PypeIt: Release 1.0.0, v1.0.0, Zenodo, doi:10.5281/zenodo.3743493
Radice, D., Perego, A., Zappa, F., & Bernuzzi, S. 2018, ApJL, 852, L29
Ramirez-Ruiz, E., Andrews, J. J., & Schrøder, S. L. 2019, ApJL, 883, L6
Read, J. S., Lackey, B. D., Owen, B. J., & Friedman, J. L. 2009, PhRvD, 79, 124032
Rest, A., Stubbs, C., Becker, A. C., et al. 2005, ApJ, 634, 1103
Richmond, M., Treffers, R. R., & Filippenko, A. V. 1993, PASP, 105, 1164
Roberts, L. F., Kasen, D., Lee, W. H., & Ramirez-Ruiz, E. 2011, ApJL, 736, L21
Rossi, E., Lazzati, D., & Rees, M. J. 2002, MNRAS, 332, 945
Rosswog, S., Piran, T., & Nakar, E. 2013, MNRAS, 430, 2585
Ryan, G., van Eerten, H., MacFadyen, A., & Zhang, B.-B. 2015, ApJ, 799, 3
Safarzadeh, M., Berger, E., Leja, J., & Speagle, J. S. 2019, ApJL, 878, L14
Savchenko, V., Ferrigno, C., Kuulkers, E., et al. 2017, ApJL, 848, L15
Schechter, P. 1976, ApJ, 203, 297
Schechter, P. L., Mateo, M., & Saha, A. 1993, PASP, 105, 1342
Schlafly, E. F., & Finkbeiner, D. P. 2011, ApJ, 737, 103
Schrøder, S. L., Batta, A., & Ramirez-Ruiz, E. 2018, ApJL, 862, L3
Scolnic, D., Casertano, S., Riess, A., et al. 2015, ApJ, 815, 117
Secrest, N. J., Dudik, R. P., Dorland, B. N., et al. 2015, ApJS, 221, 12
Shappee, B. J. 2014, PhD thesis, The Ohio State Univ.
Shappee, B. J., Prieto, J. L., Grupe, D., et al. 2014, ApJ, 788, 48
Shappee, B. J., Simon, J. D., Drout, M. R., et al. 2017, Sci, 358, 1574
Shibata, M., & Taniguchi, K. 2006, PhRvD, 73, 064027
Shingles, L., Smith, K. W., Young, D. R., et al. 2021, TNSAN, 7, 1
Siebert, M. R., Foley, R. J., Drout, M. R., et al. 2017, ApJL, 848, L26
Silverman, J. M., Kong, J. J., & Filippenko, A. V. 2012, MNRAS, 425, 1819
Singer, L. P., Chen, H.-Y., Holz, D. E., et al. 2016a, ApJL, 829, L15
Singer, L. P., Chen, H.-Y., Holz, D. E., et al. 2016b, ApJS, 226, 10
Singer, L. P., & Price, L. R. 2016, PhRvD, 93, 024013
Smartt, S. J., Chen, T. W., Jerkstrand, A., et al. 2017, Natur, 551, 75
Smith, K. W., Smartt, S. J., Young, D. R., et al. 2020, PASP, 132, 085002
Soares-Santos, M., Annis, J., Herner, K., et al. 2019b, GCN, 25486, 1
Soares-Santos, M., Palmese, A., Hartley, W., et al. 2019c, ApJL, 876, L7
Soares-Santos, M., Tucker, D., Allam, S., et al. 2019a, GCN, 25336, 1
Srivastav, S., Huber, M., Smartt, S. J., et al. 2019, GCN, 25417, 1
Stahl, B. E., Zheng, W., de Jaeger, T., et al. 2019, MNRAS, 490, 3882
Stetson, P. B. 1987, PASP, 99, 191
Stewart, A., Dobie, D., Murphy, T., et al. 2019a, Transient Name Server Discovery Report, 2019-1637
Stewart, A., Dobie, D., Murphy, T., et al. 2019b, GCN, 25487, 1
Stone, N. C., Metzger, B. D., & Haiman, Z. 2017, MNRAS, 464, 946
Swift, J., & Vyhnal, C. 2018, RTSRE, 1, 281
Swift, J., Yin, Y., Kilpatrick, C. D., et al. 2019, GCN, 25351, 1
Tan, H., Noronha-Hostler, J., & Yunes, N. 2020, PhRvL, 125, 261104
Tanaka, M., Kato, D., Gaigalas, G., & Kawaguchi, K. 2020, MNRAS, 496, 1369
Tanvir, N. R., Levan, A. J., Fruchter, A. S., et al. 2013, Natur, 500, 547
Tanvir, N. R., Levan, A. J., González-Fernández, C., et al. 2017, ApJL, 848, L27
Tews, I., Pang, P. T. H., Dietrich, T., et al. 2021, ApJL, 908, L1
Thakur, A. L., Dichiara, S., Troja, E., et al. 2020, MNRAS, 499, 3868
Thorne, K. S. 1997, arXiv:gr-qc/9704042
Tonry, J., & Davis, M. 1979, AJ, 84, 1511
Troja, E., Piro, L., van Eerten, H., et al. 2017, Natur, 551, 71
Tucker, D., Allam, S., Wiesner, M., et al. 2019b, GCN, 25379, 1
Tucker, D., Butner, M., Wiesner, M., et al. 2019a, GCN, 25484, 1
Valenti, S., Howell, D. A., Stritzinger, M. D., et al. 2016, MNRAS, 459, 3939
Vasylyev, S., Stahl, B., Zhang, K. D., et al. 2019a, GCN, 25353, 1
Vasylyev, S., Stahl, B. E., Zhang, K. D., et al. 2019b, GCN, 25437, 1
Vasylyev, S. S., & Filippenko, A. V. 2020, ApJ, 902, 149
Véron-Cetty, M. P., & Véron, P. 2010, A&A, 518, A10
Vieira, N., Ruan, J. J., Haggard, D., et al. 2020, ApJ, 895, 96
Watson, A. M., Butler, N. R., Lee, W. H., et al. 2020, MNRAS, 492, 5916
Way, M. J., Quintana, H., Infante, L., Lambas, D. G., & Muriel, H. 2005, AJ, 130, 2012
Wiesner, M., Butner, M., Allam, S., et al. 2019a, GCN, 25596, 1
Wiesner, M., Butner, M., Tucker, D., et al. 2019b, GCN, 25540, 1
Wu, X., Bao, S., Shen, H., & Xu, R. 2021, PhRvC, 104, 015802
Wu, Y., & MacFadyen, A. 2018, ApJ, 869, 55
Wu, Y., & MacFadyen, A. 2019, ApJL, 880, L23
Wyatt, S. D., Tohuvavohu, A., Arcavi, I., et al. 2020, ApJ, 894, 127
Yamazaki, R., Yonetoku, D., & Nakamura, T. 2003, ApJL, 594, L79
Zackay, B., Ofek, E. O., & Gal-Yam, A. 2016, ApJ, 830, 27
Zevin, M., Spera, M., Berry, C. P. L., & Kalogera, V. 2020, ApJL, 899, L1
Zhang, N.-B., & Li, B.-A. 2020, ApJ, 902, 38
Zheng, W., Filippenko, A. V., Mauerhan, J., et al. 2017, ApJ, 841, 64
Zhou, R., Newman, J. A., Mao, Y.-Y., et al. 2021, MNRAS, 501, 3309
Zonca, A., Singer, L., Lenz, D., et al. 2019, JOSS, 4, 1298